

1

2 This manuscript is a EarthArxiv preprint and had been submitted for publication in the **Basin**
3 **Research**. Please note that this manuscript has **not been peer-reviewed**. Subsequent versions
4 of this manuscript may, thus, have slightly different content. If accepted, the final version of
5 this manuscript will be available via the “Peer-reviewed Publication DOI” link on the right-
6 hand side of this webpage. Please feel free to contact any of the authors directly; We welcome
7 your feedback.

8

9 Origin and kinematics of a basin-scale, non-polygonal, layer-bound
10 normal fault system in the Levant Basin, eastern Mediterranean

11 Amir Joffe^{1*}, Christopher A-L. Jackson², Josh Steinberg³, Rebecca E. Bell¹, Yizhaq

12 Makovsky⁴

13 1. Basins Research Group (BRG), Department of Earth Science and Engineering, Imperial
14 College London, South Kensington Campus, SW7 2BP, UK

15 2. Department of Earth and Environmental Sciences, The University of Manchester,
16 Williamson Building, Oxford Road, Manchester, M13 9PL, UK

17 3. Ratio Energies, Tel-Aviv, Israel

18 4. Dr. Moses Strauss Department of Marine Geoscience, CSMS, University of Haifa,
19 Haifa, Israel

20 *Corresponding author: amir.joffe18@imperial.ac.uk

21 **Acknowledgments**

22 We would like to thank Ratio Energies for their financial support of Amir Joffe's PhD and for
23 providing the data for this study. We thank Ratio Energies partners, Delek Drilling and
24 Chevron, for approving access to the data and the publication of this manuscript. We extend
25 out thanks to Emerson for sponsoring Paradigm software to the Applied Marine Exploration
26 Laboratory, University of Haifa. We would also like to thank Schlumberger for sponsoring
27 Petrel software, and Geoteric for their academic licenses for Imperial College. Kul Karcz, Omri
28 Shitrit, Yedidia Gellman, Or Bialik, and Mark Ireland for fruitful discussion during the
29 preparations of this manuscript.

30 **Data Availability Statement**

31 The data is not publicly available due to confidentiality agreements.

32

Abstract

34 Polygonal, layer-bound normal faults can extend over very large areas ($>2,000,000 \text{ km}^2$) of
35 sedimentary basins. Best developed in very fine-grained rocks, these faults are thought to form
36 during early burial in response to a range of diagenetic processes, including compaction and
37 water expulsion. Local deviations from this idealised polygonal pattern are common; however,
38 basin-scale, layer-bound faults with non-polygonal map-view are not well-documented and
39 accordingly, their genesis is not well-understood. In this study we use 3D seismic reflection
40 data, biostratigraphy, and well-logs from the Southern Levant Basin, offshore Israel, to develop
41 an age-constrained seismic-stratigraphic framework and determine the geometry and
42 kinematics of such basin-scale fault system. The faults tip-out downwards along an Eocene
43 Unconformity, but unlike layer-bound faults in the Northern Levant Basin, they do not reach
44 the base of the Messinian evaporites, instead tipping-out upwards at the top Langhian. On
45 average, the faults in the Southern Levant Basin are 6.3 km long, have an average throw of 120
46 m, and consistently strike NW-SE. Throw-depth plots, accompanied by thickness changes,
47 indicate the faults nucleated as syn-depositional faults in a mudstone-dominated unit, and are
48 spatially and kinematically associated with a WSW-ESE-striking strike-slip fault. Unlike true
49 polygonal faults, these faults propagated through ~ 2 km-thick sandstone-dominated Oligocene-
50 Miocene strata. Whereas previous studies from the Northern Levant Basin associate fault
51 nucleation and growth with burial-related diagenesis, the sandstone-dominated character of the
52 Oligocene-Miocene suggests that this process cannot be readily applied to the Southern Levant
53 Basin. Instead, we highlight potential tectonic events that occurred during and may have
54 triggered thin-skinned extension at times of fault growth. Layer-bound normal faults therefore
55 should be considered in the geodynamic and structural context of the basin in which they
56 formed.

1. Introduction

58 Layer-bound normal faults (defined as faults that are vertically restricted within discrete
59 stratigraphic units and do not offset the basement) are found in sedimentary rocks throughout
60 the geological record. One of the most common types of layer-bound faults are polygonal
61 faults. These relatively small ($<200\text{-}300$ m tall) low-displacement (<100 m) normal faults are
62 found in over 150 basins around the world, forming a mostly polygonal plan-view system over
63 extremely large area ($>2,000,000 \text{ km}^2$) (Cartwright, 2011). The faults are confined within
64 discrete stratigraphic units called tiers, detached from the acoustic basement (Cartwright et al.,

65 2003). These tiers are commonly tens to hundreds of meters thick, predominantly often
66 dominated by very fine-grained, smectite-rich claystone or chalk, and are bounded by
67 sandstone-rich units or other types of detachment layers (Cartwright and Lonergan, 1996;
68 Cartwright and Dewhurst, 1998; Dewhurst et al., 1999). Their unique polygonal planform
69 suggest growth within an isotropic stress field (i.e., $\sigma_1(\text{vertical}) > \sigma_2 = \sigma_3$), with this
70 polygonal planform being highly sensitive to local changes in the prevailing stress regime. For
71 example, changes in host rock dip, and stress perturbations around salt diapirs, pockmarks, and
72 even deep-water channels all can alter the faults polygonal planform, causing them to become
73 locally aligned or radially disposed (Goult, 2002, 2008; Ireland et al., 2011; Carruthers et al.,
74 2013; Morgan et al., 2015). Even in these cases, fault nucleation and growth are assumed to be
75 triggered by the same, early burial-related diagenetic process as inferred for true polygonal
76 faults. Whereas their kinematics are fairly well understood, and there is a general agreement
77 they form by post-burial diagenetic processes involving dewatering in fine-grained clays and
78 chalk, the exact mechanism responsible for their development is still under debate (Cartwright
79 and Lonergan, 1996; Goult, 2008; Cartwright, 2011; Wrona et al., 2017; King and Cartwright,
80 2020).

81 One particularly striking example of a basin-scale (~70,000 km²), non-polygonal layer-bound
82 fault system, for which the diagenetic model has previously been proposed, is the “piano-key”
83 fault system of the Levant Basin, eastern Mediterranean (Kosi et al., 2012; Ghalayini et al.,
84 2017). Comprised of NW-striking, mostly non-polygonal, linear (i.e., one single dominant
85 orientation) faults, this system covers the entire Levant Basin, displacing the >2 km thick
86 Oligocene-Miocene strata (Ghalayini et al., 2017). By integrating seismic attribute analysis and
87 throw measurements along the faults surface, the spatial and temporal evolution of the fault
88 system has been analysed in the Northern Levant Basin (Figure 1) (Kosi et al., 2012; Hawie et
89 al., 2013; Ghalayini et al., 2017; Ghalayini and Eid, 2020). On the basis of the faults layer-
90 bound geometry, a small portion of polygonally-shaped faults in the system, and the lack of
91 known extension events at times of presumed fault nucleation, Ghalayini et al. (2017)
92 associated the piano-key faults with the same dewatering, diagenetic mechanism often inferred
93 to drive polygonal fault nucleation and growth. The dominant NW strike of the piano-key faults
94 reflected their development in an anisotropic (rather than isotropic) stress field (Ghalayini et
95 al., 2014, 2017).

96 Piano-key faults are also documented in the Southern Levant Basin, displacing a thick
97 sandstone-rich, Oligocene-Miocene sequence (see detailed description in sub-section 2.0)

98 (Steinberg et al., 2011; Needham et al., 2017; Craik and Ben-Gai, 2019; Gouliotis, 2019; Karcz
99 et al., 2019; Ortega et al., 2019). In this study we constrain the evolution of the piano-key faults
100 in the Southern Levant Basin, before proposing a mechanical model that considers the
101 lithological variability of the faulted sequence and the broader geo-dynamic setting of the basin
102 at the time of fault formation. To do this we use high-quality, 3D seismic reflection data,
103 chronostratigraphic markers, and well-logs from six offshore wells. This allows us to (1) create
104 a detailed, age-constrained, stratigraphic framework; (2) constrain the lithological variability
105 of the different units within the faulted Oligo-Miocene; (3) measure the geometrical properties
106 of individual faults and the fault system as a whole; (4) determine the faults kinematics; (5)
107 discuss possible mechanical models for the formation of the piano-key faults, while also
108 considering the geo-dynamic events occurring at the basin during fault nucleation and growth.
109 The results of our study indicate that basin-scale, layer-bound normal fault systems can develop
110 in sandstone-dominated sequences. We also argue that in this specific case, the previously
111 proposed diagenetic mechanism may not be applicable (Ghalayini et al., 2017; Ghalayini and
112 Eid, 2020), and those late Miocene regional tectonic events which shaped the Levant Basin
113 may have played a role.

114 **2. Geological Setting**

115 The Levant Basin is located in the eastern Mediterranean and is bordered by the Cyprus
116 subduction arc to the north, the Eratosthenes Seamount to the west, and the continental margin
117 of Egypt, Israel, Lebanon, and Syria to the south and east (Figure 1A). We here follow the
118 arbitrary division of the basin into the Southern and Northern Levant Basins approximately
119 along the Israel-Lebanon maritime border (Ben-Gai, 2018) (Figure 1A). The basin's unique
120 location within a triple-junction of the Eurasia, Arabia, and Africa plates means it evolved in
121 response to a complex series of tectonic-stratigraphic events.

122 The basin initially formed in response to Permian, Triassic, and Early Jurassic rifting,
123 associated with multi-phase, NW-SE-oriented extension, thinning of the continental crust and
124 the formation of NE-SW-striking normal faults (Garfunkel and Derin, 1984; Garfunkel, 1998;
125 Gardosh and Druckman, 2006; Robertson, 2007; Gardosh, Druckman, Buchbinder, and
126 Rybakov, 2008; Gardosh et al., 2010; Sagy et al., 2015; Granot, 2016). Following this, passive
127 margin conditions prevailed until the Late Cretaceous, during which time a shallow marine
128 carbonate platform was established along the basin margin (Garfunkel and Derin, 1984;
129 Garfunkel, 1998; Gardosh and Druckman, 2006; Gardosh, Druckman, Buchbinder, and

130 Rybakov, 2008; Gardosh and Tannenbaum, 2014). Late Cretaceous convergence between the
131 African and Eurasian plates resulted in the formation of a north-dipping subduction zone along
132 the Cyprus Arc (Robertson, 1998a; Gardosh, Druckman, Buchbinder, and Rybakov, 2008;
133 Morag et al., 2016). Within the Southern Levant Basin, compressional stresses related to
134 ongoing subduction caused large-scale folding above the pre-existing, rift-related normal faults
135 (Krenkel, 1924; Freund, 1975; Cohen et al., 1990; Druckman, 1994; Garfunkel, 2004; Sagy et
136 al., 2018). Forming part of the ‘Syrian Arc’ (Krenkel, 1924), these folds are most prominent
137 onshore and along the basin’s eastern margin, where high-amplitude, short wave-length
138 anticlines are developed (i.e., 10-30 km long, 5-10 km wide, and an amplitude of >1 km) (Eyal,
139 1996; Walley, 1998; Gardosh, Druckman, Buchbinder, and Rybakov, 2008). This first pulse of
140 Syrian Arc-related folding stopped by the Eocene, during a time characterised by deepening
141 and the deposition of deep-water chalk and marls across much of the Middle East (Garfunkel,
142 1998; Ziegler, 2001; Bar et al., 2013; Sagy et al., 2018; Steinberg et al., 2018).

143 In addition to witnessing a second Syrian-Arc related folding event (Syrian Arc II) (Robertson,
144 1998a; Walley, 1998; Gardosh, Druckman, Buchbinder, and Calvo, 2008; Needham et al.,
145 2017; Sagy et al., 2018), the Oligo-Miocene recorded a drastic change in depositional
146 environment within the basin, from deep-water carbonates to deep-water clastics, resulting in
147 the Eocene Unconformity (Steinberg et al., 2011). This change created drastic increase in
148 sedimentation rates, peaking between ~24-12 Ma (~900 m/Myr), two orders of magnitude
149 higher than the pre-Oligocene period (~5 m/Myr) (Torfstein and Steinberg, 2020). The cause
150 for this drastic and immediate change was linked to a series of geodynamic events that exposed
151 large expanses of previously submerged areas, which then formed significant clastic sediment
152 sources. These events include: (1) regional uplift of the eastern margin that exposed the Arabian
153 Plateau, initiating large-scale, NW-directed drainage system into the retreating Levant (Zachos
154 et al., 2001; Ziegler, 2001; Gvirtzman et al., 2011; Bar et al., 2016; Faccenna et al., 2019); (2)
155 regional doming south of the Levant basin, created by the Afar Plume, which elevated the
156 Ethiopian Plateau (31-29 Ma) (Bosworth et al., 2015); (3) Red-Sea rifting, which was initiated
157 by the Cairo Plume (23 Ma) (Bosworth et al., 2005, 2015); (4) the final stages of closure of the
158 Indian Ocean – Mediterranean Seaway (IOMS) in the Aquitanian (Bialik et al., 2019; Torfstein
159 and Steinberg, 2020); (5) the activation of the Continental Margin Fault Zone along the Levant
160 eastern margin in the Early Oligocene (Gvirtzman and Steinberg, 2012); (6) the development
161 of the Dead Sea transform in the Burdigalian (Freund, 1975; Garfunkel, 1997; Segev et al.,
162 2014; Nuriel et al., 2017); and (7) the local uplift of the Judea Hills, onshore Israel (Bar et al.,

163 2013). It is not yet clear if or how all these events kinematically interacted, but it does highlight
164 that during the Oligo-Miocene, the Levant Basin was tectonically very active, and that this
165 activity could have influenced the formation and growth of the fault system considered here.

166 Restriction of the Atlantic-Mediterranean waterway during the Late Miocene (5.59 – 5.33 Ma)
167 resulted with the Messinian Salinity Crisis and the accumulation of up to ~2.5 km thick
168 evaporitic sequence in the Levant basin (Hsü et al., 1977; Krijgsman et al., 1999; Ryan, 2009).
169 After Pliocene rise of the Judea Hills and the development of the Dead-Sea Transform, the
170 easterly drainage system was disconnected from the Levant, making the River Nile the main
171 sediment source to the basin (Garfunkel, 1981; Gardosh, Druckman, Buchbinder, and Calvo,
172 2008; Gardosh, Druckman, Buchbinder, and Rybakov, 2008; Gvirtzman et al., 2014, 2015; Bar
173 et al., 2016; Zucker et al., 2019; Kanari et al., 2020).

174 2.1. The Piano Key Faults of the Northern Levant Basin

175 The piano-key fault system is composed of a NW-striking normal fault system that covers
176 ~70,000 km² offshore Lebanon, Israel, and Cyprus (Ghalayini et al., 2017). Offshore Lebanon,
177 in the Northern Levant Basin, the faults are bounded below by the Eocene Unconformity and
178 above by the base of the Messinian evaporites, displacing the Oligo-Miocene sedimentary
179 sequence (Kosi et al., 2012; Ghalayini et al., 2017; Ghalayini and Eid, 2020). Based on their
180 geometry and how fault throw varies with depth, the faults in the system offshore Lebanon
181 were divided into three main ‘types’ by Ghalayini and Eid (2020) (Figure 1). Type-1 (T1) faults
182 are predominantly located in the deep basin (Figure 1A). They are tall (~3800 m), long (6-12
183 km), linear, strike NW, and have a maximum displacement of 200-350 m (Ghalayini and Eid,
184 2020) (Figure 1B). Throw vs depth analysis, which highlights the depth of fault nucleation as
185 a function of maximum throw, revealed two throw maxima separated by a local minimum,
186 creating a “B-Type” profile (Muraoka and Kamata, 1983; Ghalayini et al., 2017). The analysis
187 indicates that T1 faults had nucleated in separate tiers, later connecting by fault tip propagation
188 (Figure 1B). The presence of growth strata in the ‘Lower-Middle Miocene Interval’ suggests
189 faults breached the surface during the Early-Middle Miocene (Reiche et al., 2014), even
190 though, we note, the faults could have nucleated at greater structural depths. Found in the
191 northernmost part of the basin, adjacent to the Latakia Ridge, Type-2 (T2) faults are small
192 (~1,000 m tall), short (2-3 km in length), and have smaller displacements than T1 faults (<60
193 m). Unlike T1, T2 faults have no observable growth strata, and their throw-depth analysis
194 creates a symmetrical, “C-type” profile that lacks any local minima (Muraoka and Kamata,
195 1983; Ghalayini and Eid, 2020) (Figure 1B). Unlike the other types of faults, T2 faults are not

196 co-linear in planform, but rather form a semi-polygonal planform (Figure 1A). Type-3 (T3)
197 faults are linear, striking NW-SE. They are found along the eastern basin margin and do not
198 displace the Eocene Unconformity or the base-Messinian (Ghalayini and Eid, 2020) (Figure
199 1B) being the smallest faults in the basin, i.e., they are <800 m tall, have <90 m of displacement,
200 and are <3 km in length. T3 faults are characterised by “C-type” throw profiles and lack growth
201 strata, similar to the T2 faults (Ghalayini and Eid, 2020).

202 The vast areal extent of the faults, alongside their layer-bound character and the polygonal
203 planform of the T2 faults, led Ghalayini et al. (2017) to suggest they formed due to compaction
204 and dewatering during shallow burial (e.g., Cartwright, 2011). In the absence of borehole data,
205 these authors inferred that the faults developed in a mudstone-dominated, very fine-grained
206 sedimentary sequence, typical of polygonal fault systems. They argued that the throw-
207 minimum on the T1 faults and their “B-type” throw-depth profiles is associated with a
208 sandstone-rich, basin floor fan (Ghalayini and Eid, 2020) (Figure 1C). Similar observations
209 were made in the Måløy Slope, offshore western Norway, where a 92 m sandstone body
210 separated two mudstone dominated tiers, leading to a local minimum on throw-depth profiles
211 (Jackson et al., 2014). However, unlike the example from the Northern Levant Basin, the
212 relationship between fault geometry and distribution, and host rock composition, can be
213 directly determined by borehole data in the case of the Måløy Slope.

214 **3. Dataset**

215 The available dataset consists of seven deep-water wells, and one 3D Pre-Stack Depth Migrated
216 (PSDM) seismic reflection volume covering 2355 km² in water depth of ~1.5 km offshore
217 Israel (Figure 2A). The seismic data were acquired in 2009 and processed in 2010 by Petroleum
218 Geo-Services. Reprocessing of the survey in 2019 by WesternGeco focused on the faulted
219 Oligo-Miocene sequence, with a final bin size of 25x25 m. Inlines and crosslines are oriented
220 NE-SW and NW-SE respectively (i.e., parallel, and perpendicular to the faults orientation). In
221 figures red represent positive amplitudes peaks, indicating an increase in acoustic impedance
222 with depth, and blue represent negative amplitude troughs, indicating a decrease in acoustic
223 impedance.

224 The available wells targeted the Oligo-Miocene sequence, with X-2 terminating just above the
225 faulted sequence. X-1 is the deepest well, reaching as deep as the Eocene unconformity (i.e.,
226 near the basal tips of the studied faults; Figure 2C). All wells have full well-log suites and
227 lithostratigraphic markers.

4. Methodology

229 We used lithostratigraphic markers, and chronostratigraphic data from dated cutting samples
230 (Torfstein and Steinberg, 2020) to constrain the age of nine sub-evaporite reflections (Figure
231 2B). The deepest reflection mapped in this study was not penetrated by the wells, but following
232 other seismic-stratigraphic frameworks, which correlated onshore data to the shallow offshore
233 in the Southern Levant Basin (Gardosh et al., 2008b; Steinberg et al., 2011, 2018), we interpret
234 it as base Senonian, based on its characteristic seismic expression (Steinberg et al., 2018)
235 (Figure 2B). We used the Geoteric HDFD spectral decomposition workflow to enhance the
236 subtle structural elements (Eckersley et al., 2018), most importantly the WSW-ENE-striking
237 fault and its associated splays.

238 Constraining the sub-evaporite lithological variability was performed by integration of log-
239 based petrophysical analysis and cutting samples. Along our depth range of interest, samples
240 were collected every 3 m, then washed on the drilling rig, and the lithologies averaged by the
241 well site geologist (Figure 3). The integration of a conventional log-based approach along with
242 cutting samples were vital to our analysis as the Oligo-Miocene comprises mud-rich sandstone,
243 making wireline-only analysis potentially problematic (Christensen and Powers, 2013). Some
244 of these complexities include: (1) the effect that the high-salinity, water-based mud used while
245 drilling in most wells had on the logging tools; and (2) in most cases, the clay-rich layers are
246 not thick enough (i.e., <4 m) to be fully resolved by the logging tools within the reservoir
247 interval, and when compared to the overlying limestone-mudstone sequence, the GR_{shale}
248 baseline overestimates shale volumes (Christensen and Powers, 2013). For these reasons we
249 have compared gamma-ray, neutron-density, and cutting samples to create a simplified
250 lithology column for each well, indicating the main lithological variability present within the
251 Oligo-Miocene host rock (Figure 3).

252 Kinematic analysis was performed on 136 faults in the study area. The spatial and temporal
253 evolution of the different structural elements, including the NW-SE-striking faults, were
254 determined by following the methodology of Jackson et al. (2017): (1) depth-structure maps
255 were used to highlight the current geometry of the sedimentary sequence. These maps were
256 then used to generate thickness (isopach) maps that highlight the timing of syn-depositional
257 structural activity: across-fault thickening indicates syn-sedimentary fault growth, and thinning
258 across the Leviathan High indicates periods of syn-depositional folding (Thorsen, 1963;
259 Jackson and Rotevatn, 2013; Jackson et al., 2017); (2) strike-parallel throw profiles (t-x) were

260 used to visualise the spatial distribution of strain within the fault system (Walsh and Watterson,
261 1990; Peacock and Sanderson, 1991, 1996; Childs et al., 1995, 2019). By measuring the throw
262 along a fault length (we measured throws every 250 m, regardless of the fault length), t-x
263 profiles can help indicate kinematic interaction between and the linkage of faults within the
264 system (Peacock and Sanderson, 1991, 1996; Dawers and Anders, 1995; Nicol et al., 2010;
265 Jackson and Rotevatn, 2013; Childs et al., 2019). This analysis is specifically beneficial when
266 the piano-key faults are compared to polygonal faults, as polygonal faults are thought to have
267 a higher degree of fault interaction and linkage (i.e., the system is more mature) with depth
268 (Cartwright, 2011); (3) dip-parallel throw profiles (t-z) were used to understand the role dip-
269 linkage and mechanical stratigraphy had on fault growth and ultimate geometry (Muraoka and
270 Kamata, 1983; Peacock and Sanderson, 1991; Childs et al., 1996; Cartwright et al., 1998;
271 Rykkelid and Fossen, 2002; Baudon and Cartwright, 2008; Roche et al., 2012; Jackson and
272 Rotevatn, 2013; Jackson et al., 2017; Rotevatn et al., 2019). T-z plots also help us infer the
273 depth and correlative geological period at which the faults nucleated (Barnett et al., 1987;
274 Walsh and Watterson, 1988; Nicol et al., 1996a; Walsh et al., 2003; Jackson and Rotevatn,
275 2013; Wrona et al., 2017). We extracted t-z plots from the position of maximum throw, as
276 identified on the t-x plots. Similar techniques have been applied in previous studies to highlight
277 how sandstone intervals separate polygonal fault tiers and how they are themselves
278 characterised by a local minima (Lonergan et al., 1998; Stuevold et al., 2003; Cartwright, 2011;
279 Jackson et al., 2014; Ghalayini et al., 2017; Turrini et al., 2017; Wrona et al., 2017); (iv)
280 expansion index (EI) plots (i.e., hangingwall vertical thickness of a stratigraphic package
281 divided by its footwall vertical thickness) were constructed to identify growth strata and hence
282 determine if faults breached the surface during their development (Jackson et al., 2017).
283 Growth strata are highlighted where $EI > 1$ (Thorsen, 1963; Cartwright et al., 1998; Tvedt et al.,
284 2013; Robson et al., 2017). EI plots were constructed at the same sites where throw-depth plots
285 were taken.

286 **5. Results**

287 Here we integrate our observations of seismic facies variability with drilling data to constrain
288 the age and lithology of our new, sub-evaporite, seismic-stratigraphic framework. Thickness
289 changes within different units are also highlighted, which help infer the timing and pattern of
290 deformation. We then integrate this with our detailed analysis of the geometry and kinematics
291 of the NW-SE-striking, layer-bound faults (sections 5.3 and 5.4), such that we can ultimately
292 propose a mechanical model for fault development (Section 6).

293 5.1. Seismic-Stratigraphic Framework and Integration with Drilling Data

294 In addition to the base-evaporite horizon, we interpreted 10 pre-evaporite horizons to constrain
295 the 10 seismic-stratigraphic units (Figure 1). Each section below begins with a description of
296 the unit seismic facies and lithology, the latter derived from drilling data. Then, the current
297 geometry of its bounding upper surface and if present, any thickness changes within the unit
298 are also characterised. This structural framework provides the foundation for the kinematic
299 analysis linking the timing of layer-bound faulting and other regional tectonic events in the
300 Southern Levant Basin.

301 *Unit 1: Pre-Senonian*

302 Unit 1 is characterised by sub-horizontal, continuous, moderate-amplitude reflections and is
303 capped by the bright, continuous, ‘Senonian Unconformity’ horizon (Figure 2C). On the basis
304 of published onshore and shallow offshore wells (i.e., no wells penetrated this unit in the deep-
305 offshore), the Mid-Jurassic to Senonian unit comprises deep-water clastics, and pelagic and
306 hemipelagic carbonates (Gardosh, Druckman, Buchbinder, and Rybakov, 2008; Gardosh et al.,
307 2011). The top of unit 1 outline the large, triangular Leviathan High, which is located at the
308 centre of the study area. The high is bounded to the north by an ENE-WSW-striking fault and
309 to the south by a NE-striking, SE-dipping monocline (Figure 4A). No thickness analysis is
310 presented for this unit as we did not have any lower boundary reflection to constrain this unit.

311 *Unit 2: Senonian - Eocene (33.9)*

312 Unit 2 is characterised by chaotic, mostly transparent or low-amplitude seismic reflections and
313 is capped by the bright, continuous, ‘Eocene Unconformity’ (33.9 Ma) (Figure 2). Our
314 lithological analysis of X-1 well indicate that Unit 2 is composed of deep-water chalk and
315 marls, which is in agreement with previous studies of the deep Levant Basin (Figure 3)
316 (Gardosh, Druckman, Buchbinder, and Calvo, 2008; Steinberg et al., 2011; Gardosh and
317 Tannenbaum, 2014). The Leviathan High is still well-expressed at the top of Unit 2, with NW-
318 striking faults are also developed at this level (Figure 4B). Unit 2 (Figure 5A) thins across the
319 Leviathan High and it gently thickens from the footwall to the hanging wall of the faults. The
320 unit age corresponds to the same age as the Syrian Arc I, therefore the thickness changes seen
321 here suggest an uplift/folding of the Leviathan High alongside fault activity during this time.

322 *Unit 3: Rupelian – Early Chattian (33.9 – 24.07 Ma)*

323 Characterised by sub-horizontal, semi-transparent, moderate amplitude seismic reflections,
324 Unit 3 is capped by the bright, semi-continuous Intra-Chattian horizon (24.07 Ma) (Figure 2).

325 The lithological analysis from X-1 well shows that this deep Oligocene unit is composed by
326 thin (~5 m thick) sandstone beds within a mostly mudstone-dominated sequence (Figure 3).
327 The Leviathan High is also well-expressed at the top of Unit 3, with the NW-striking faults
328 also well developed (Figure 4C). Degradation in the imaging quality at this depth interval make
329 the Intra-Chattian horizon difficult to map (Figure 4C), as expressed in the southern portion of
330 the thickness map for Unit 3 (Figure 5B). However, it is still clear that Unit 3 is broadly tabular
331 and of uniform thickness, indicating the main tectonic event(s) occurring during in Unit 2 had
332 largely stopped (Figure 5B).

333 *Unit 4: Late Chattian (24.07 – 23.02 Ma)*

334 Unit 4 is characterised by a sub-horizontal, mostly continuous, moderate to high amplitude
335 seismic facies, and is capped by the semi-continuous, moderate to low amplitude Top
336 Oligocene horizon (23.02 Ma) (Figure 2). Like Unit 3, Unit 4 is composed by alternations of
337 sandstone and mudstone (Figure 3). The top of Unit 4 still shows the Leviathan High and the
338 NW-SE-striking faults (Figure 4D). As with Unit 3, Unit 4 is isopachous (Figure 5C).

339 *Unit 5: Aquitanian (23.02 – 21.2 Ma)*

340 Unit 5 is composed of sub-horizontal, continuous, moderate amplitude reflections that become
341 stronger upwards, until reaching the bright, continuous, regionally extensive Top Aquitanian
342 horizon (21.2 Ma) (Karcz et al., 2019) (Figure 2). Penetrated by five of the six wells, Unit 5 is
343 also composed of alternating sandstone and mudstone, like Units 3 and 4 (Figure 3). The
344 Leviathan High, the NW-SE-striking faults and the WNW-ENE-striking strike-slip faults are
345 all very clearly expressed at the top Unit 5 map (Unit 4E). Like Unit 3 and 4 Unit 5 is broadly
346 isopachous (Figure 5D).

347 *Unit 6: Early Burdigalian (21.2 – 17.54 Ma)*

348 Unit 6 is characterised by sub-horizontal, semi-continuous, moderate amplitude seismic
349 reflections, capped by the moderate amplitude Intra-Burdigalian horizon (17.54 Ma) (Figure
350 2). Unit 6 is more sandstone-rich than the deeper units with Net-to-Gross of 70% (Karcz et al.,
351 2019), and it contains the stratigraphically youngest sandstones present within the faulted units
352 (Figure 3). The high Net-to-Gross of this unit has substantial impact of the fault-growth model
353 we present later in this manuscript (see section 6.1.2.). The top of Unit 6 continues to show the
354 Leviathan High and the NW-SE-striking faults (Figure 4F). Unit 6 gently thins towards the
355 WSW-ENE-striking strike-slip fault, but no thickness changes are seen across the faults (Figure

356 5E). This NW thinning trend towards the strike-slip fault may suggest a renewed tectonic
357 activity in the study area.

358 *Unit 7: Late Burdigalian – Middle Langhian (17.54 – 14.4 Ma)*

359 Unlike the units below, Unit 7 is characterised by semi-transparent, low to medium amplitude
360 seismic reflections, capped by the continuous, bright Intra Langhian horizon (14.4 Ma) (Figure
361 2). Unit 7 is mudstone-dominated and contains thin (<5 m thick) carbonate beds; sandstone is
362 notably absent (Figure 3). Because the carbonate beds are relatively thin, they are not clearly
363 detected in well-logs; however, they are observed in all six well-site analyses, documented in
364 cutting samples and composite logs. In addition to the triangular Leviathan High and the NW-
365 SE-striking faults, the Intra-Langhian structural map also shows a system of polygonally
366 arranged depressions (Figure 6), which locally become concentric around the Tamar anticline
367 (Figure 6C). Critically; (i) this polygonal fabric appears only above Unit 7's growth strata
368 associated with the NW-striking faults (Figure 6B); and (ii) the faults displace the polygonal
369 fabric (Figure 6D&E), suggesting the latest activity of the depressions post-dated the formation
370 of the faults. Besides thickness changes associated with the NW-striking faults (Figure 7), Unit
371 7 also shows thinnings across the Leviathan High (Figure 5F), indicating significant tectonic
372 activity period.

373 In detail, flattening the Top Langhian horizon reveals a significant intra-formational onlap
374 horizon within Unit 7 (Figure 8). This horizon, which is dated as Late Burdigalian (~15 Ma),
375 divides Unit 7 into two (Figure 8). The lower sub-unit 7 (7a) is broadly tabular and seismic
376 reflections are continuous over the Leviathan High (Figure 8C & E), whereas the upper sub-
377 unit (7b) onlaps this Late Burdigalian horizon on both sides of the Leviathan High (Figure 8
378 C & D).

379 *Unit 8: Late Langhian (14.4 – 13.82 Ma)*

380 Unit 8 is characterised by sub-horizontal, continuous high amplitude seismic reflections, and
381 is capped by a very high amplitude Top Langhian horizon (13.82 Ma) (Figure 2). Like Unit 7,
382 Unit 8 is mudstone-dominated, containing thin (< 5 m thick) carbonate beds (Figure 3). The
383 Leviathan High, and the polygonal fabric are well expressed on the top of Unit 8, while the
384 NW-SE-striking faults are not as well expressed as in the deeper units (Figure 6). Like sub-
385 Unit 7b, Unit 8 thins across the Leviathan High, with only very minor thickness changes
386 occurring across the NW-striking faults (Figure 5G). These thickness changes may suggest the
387 tectonic activity which started at Unit 7 is continuous through Unit 8.

388 We note that the top of Unit 8 defines an unconformity, with Serravallian strata missing in the
389 two wells studied by Torfstein and Steinberg (2020). Those authors show that Unit 8 is capped
390 by a mudstone-rich, carbonate-poor Tortonian (Unit 9), suggesting the top of the Langhian
391 coincides with the global Miocene Carbonate Crash event, and concluding that the
392 unconformity resulted from a of a large-scale carbonate dissolution event. This dissolution
393 event may be responsible for the polygonal patter identified at the tops of Units 7 and 8, as
394 carbonate beds were documented within both units.

395 *Unit 9: Early Tortonian (13.82 – 9.18 Ma)*

396 Unit 9 is characterised by a chaotic, low-amplitude seismic-facies which is capped by a
397 moderate amplitude, continuous Intra-Tortonian horizon (9.18 Ma) (Figure 2). Torfstein and
398 Steinberg (2020) note that Unit 9 is mudstone-rich and foraminifera- and CaCO₃-poor,
399 indicative of carbonate dissolution (see above). Because of its chaotic seismic signature, we
400 cannot say for certain whether the faults extend through Unit 9, although the top of the unit
401 does not appear to be deformed by these structures (Figure 4I). Unit 9 clearly thins across the
402 Leviathan High (Figure 5H) indicating the second tectonic activity which started at Unit 7 is
403 continuous here. The origin of this chaotic section is beyond the scope of this manuscript, but
404 we do suggest a possible correlation to similar observations made by Papamitriou et al. (2018),
405 where they suggested a similar chaotic section on the flanks of the Eratosthenes Seamount,
406 triggered by the collision between the Seamount and Cyprus.

407 *Unit 10: Late Tortonian (9.18 – 5.96 Ma)*

408 Unlike Unit 9, Unit 10 is characterised by sub-horizontal, continuous, moderate amplitude
409 seismic reflections, capped by the base-evaporites bright and continuous seismic horizon
410 (Figure 2). Unit 10 is lithologically similar to Unit 9, comprising foraminifera- and CaCO₃-
411 poor mudstone (Torfstein and Steinberg, 2020). The top of Unit 10 dips gently north-
412 westwards, although three large channels are present (Figure 4J). The NW-striking faults are
413 absent. Similar to Unit 9, Unit 10 thins across the Leviathan High (Figure 5E).

414 In summary, our dataset is dominated by the large, triangular-shaped Leviathan High and
415 numerous NW-SE-striking, layer-bound (i.e., by the Top Langhian and Base Oligocene
416 horizons) normal faults. Thickness changes are seen in two main stratigraphic intervals and
417 corresponding time periods: the first during the Senonian - Eocene, where thinning across the
418 Leviathan High is most dominant, and the second during the Burdigalian and Langhian, where
419 marked thickness changes occur not only across the Leviathan High, but also across the NW-

420 SE-striking faults. These two phases of deformation appear to have been separated by a period
421 of relative quiescence.

422 5.2. Other Prominent Structural Elements

423 In addition to the NW-striking piano-key faults and the Leviathan High described above, a
424 prominent ENE-WSW-striking fault exists across our study area along the northern edge of the
425 Leviathan High. Cross-sections across the fault indicate that it corresponds with a deep, single
426 stem which cross-cuts the entire Senonian to Oligo-Miocene sedimentary sequence (Figure
427 9A). From its single stem, splays spread in a negative flower structure along the Top Aquitanian
428 horizon (Figure 8A). Spectral decomposition along the Top Aquitanian horizons highlight this
429 WSW-ENE-striking fault, which is composed of several, similarly striking, segments (Figure
430 9C). Adjacent to these segments, the otherwise NW-SE-striking piano-key faults change their
431 strike to N-S, perpendicular and locally physically linked to the ENE-WSW-striking fault
432 system (Figure 9C). Similar geometric relationships are seen in the adjacent Karish gas field
433 (~50 km east of our study area). There, NW-striking faults abut against the ‘Karish Shear Zone’
434 (Gouliotis, 2019), a WSW-ENE-striking, dextral strike-slip fault that could be the along-strike
435 extension of the geometrically similar fault found in our study area (Stearman et al., 2021).
436 Additionally, we note two other smaller (~5 km long), ENE-WSW-striking faults at the centre
437 of the study area, where the intensity of NW-striking faults is locally higher than elsewhere
438 (Figure 9C&8E). Finally, in terms of their age, thickening of Units 7 and 8 indicates the ENE-
439 WSW-striking structure was active in the Late Burdigalian to Late Langhian (Figure 7 & 9B).

440 Similar geometrical relationships between otherwise NW-SE-striking piano-key faults and
441 WSW-ENE-striking faults are documented in the Northern Levant Basin (Ghalayini et al.,
442 2014). There, the faults change their orientation to strike in an almost N-S direction and they
443 are inferred to represent Riedel-like structures orientated at 60° from the dextral strike-slip fault
444 (Ghalayini et al., 2014). The origin of these faults is not yet clear, but Ghalayini et al. (2014)
445 suggested they may be related to a strike-slip reactivation of buried rift-related faults by the
446 dextral movement along the Dead-Sea transform.

447 5.3. NW-SE-Striking Fault Geometry and Distribution

448 We have identified, mapped, and undertaken a geometric and kinematic analysis of 136,
449 predominantly NW-SE-striking normal faults present within the Oligo-Miocene succession,
450 bounded above by the Base Oligocene and below the Top Langhian (Figure 10). The faults
451 have an average length of 6.3 km and average throw of 116 m (see section 5.4.2. for more

452 details); and are normally displaced relative to their length (Figure 9B). Most faults (61%) dip
453 to the SW, with seemingly no relationship between faults dip direction and their location,
454 except to the north of the WSW-ENE-striking fault described above, where all the layer-bound
455 faults dip SW (Figure 9A).

456 5.4. Kinematic Analysis of Layer-Bound Normal Faults

457 5.4.1. *Throw-Length (t-x) analysis*

458 Of the 136 mapped faults in the study area, 16 were not included in this analysis (or the t-z
459 analysis described below) because they extended outside of the seismic dataset and thus, we
460 could not constrain their true length. Based on their throw vs. length profile shape, the faults
461 were classified into four groups (TX1-4) (Figure 11). TX1 and TX2 are asymmetrical, with
462 maximum throw offset to the SE or the NW, respectively, of the fault centre. TX3 are
463 symmetrical, with maximum throw at the fault centre, whereas TX4 is defined by a profile
464 containing two throw maxima (Figure 11). We do not see any direct spatial correlation between
465 these groups and other structural elements; however, we do note that a change in the
466 distribution of strain with depth. For example, our analysis shows that symmetrical profiles are
467 more common with depth, i.e., whereas 37% of the faults displacing the upper boundary (Late
468 Langhian horizon) have a symmetrical throw distribution, 67% of the faults displacing the
469 lower boundary (Base Oligocene) have a symmetrical throw distribution (Figure 11). Given
470 that symmetrical profiles typify less mature faults that have developed in kinematic isolation
471 from surrounding structures, we infer a greater degree of fault interactions and higher fault
472 maturity at shallower depth (Walsh and Watterson, 1990; Nicol et al., 2010). This differs to
473 that commonly observed in polygonal faults, where a higher degree of fault interactions are
474 developed at structurally deeper depths (Cartwright, 2011).

475 5.4.2. *Throw-Depth (t-z) analysis*

476 Throw-depth profiles were constructed for the same 120 faults analysed in sub-Section 5.4.1.
477 Our analysis shows that the average t-z profile is asymmetric, with maximum throw across the
478 Intra-Burdigalian (17.54 Ma) horizon, decreasing upwards and downwards towards the fault
479 tips (Figure 12A).

480 The faults were divided into two main groups based on their vertical extent (TZ1 and TZ2).
481 TZ1 faults displace the entire Oligo-Miocene sequence, with an average length of 7.2 km, an
482 average height of 1.9 km, and an average vertical throw of 128 m (Figure 12). TZ1 throw
483 profiles are asymmetrical, with a prominent maximum throw along the Intra-Burdigalian

484 horizon (Figure 12A). From this maximum, the throw profile decreases almost linearly both
485 upwards to the base of the Lower Tortonian chaotic unit (Unit 9), and downwards to the Upper
486 Chattian/Eocene units. TZ2 faults are smaller (average length of 4.2 km and a maximum throw
487 of 80 m), their lower tip does not displace the Intra-Chattian horizon, and they exhibit a more
488 symmetrical throw profile (Figure 12). Spatially, 70% of the mapped faults in the study area
489 are TZ1, with TZ2 mostly located along the high's flanks (Figure 12C).

490 Compared to throw-depths plots by Ghalayini et al. (2017) and Ghalayini and Eid (2020) from
491 the Northern Levant Basin offshore Lebanon, TZ1 faults are similar to their Type-1 faults and
492 TZ2 are similar to their Type-3 faults (Figure 1 & 12). Whereas some similarities could be seen
493 with regards to their throw-depth plots, the faults in the Northern and Southern Levant Basin
494 do have their differences. Unlike Type-1 faults offshore Lebanon, TZ1 faults offshore Israel
495 do not offset the base-Messinian evaporite, making them smaller than the Type-1 faults
496 offshore Lebanon (height of 1.9 km vs 3.8 km), and with smaller vertical throw (120 m vs ~250
497 m). TZ2 and Type-3 faults do have very similar geometrical properties, but unlike Type-3 faults
498 offshore Lebanon who are located along the basin margin (Figure 1), TZ2 faults are located in
499 the deep basin (Figure 12).

500 5.4.3. *Expansion Index*

501 Expansion Index (EI) for the 120 faults analysed yielded $EI > 1$ for Unit 7 (17.54 – 14.4 Ma)
502 and Unit 8 (14.4 -13.82 Ma), with $EI = 1$ for Unit 3 (33.9 – 24.07 Ma) (Figure 13A). Values $<$
503 1 is seen in the other units, possibly highlighting the difficulty associated with the interpretation
504 of the bounding horizons (Figure 13A) (see further details in section 5.1). EI results strengthen
505 our observations from sub-section 5.4.2., whereby all the faults, regardless of bottom tip depth,
506 nucleated during the Late-Burdigalian, with possible continued activation during the Langhian
507 (Figure 13B).

508 To summarize our kinematic results, using thickness maps, throw-length profiles, throw-depth
509 profiles, and expansion index we determine the piano-key faults in the Southern Levant Basin
510 had nucleated as syn-depositional faults, breaching the seabed and accumulating growth strata,
511 during the Late Burdigalian. After fault nucleation, vertical tip propagation had played a key
512 role in the final geometry of the faults, as some had propagated all the way to the Base-
513 Oligocene where they terminate (TZ1), while others did not (TZ2).

514 6. Discussion

515 6.1. Mechanical model for the formation of the piano-key faults

516 We have shown that the non-polygonal layer-bound faults in our study area have all nucleated
517 as syn-sedimentary faults during the Late Burdigalian. The faults probably nucleated just below
518 the seabed, in the mudstone dominated Unit 7, and propagated through the underlying siltstone
519 and sandstone dominated units. This kinematic finding raises questions regarding their origin:
520 (1) how can a diagenetic induced fault system, so strongly linked to very fine-grained sediments
521 and sensitive to changes in host rock composition, propagate through a ~2 km thick sandstone
522 rich host rock? (2) what occurred in the basin during the time of fault growth that caused their
523 initial nucleation? (3) why are the faults so linear, striking NW-SE, perpendicular to the basin
524 margin? To address these questions, we here describe possible mechanical models for their
525 formation and discuss their implications.

526 6.1.1. *Diagenetic model*

527 Previous studies from the Northern Levant Basin, offshore Lebanon suggested that the piano-
528 key faults nucleated and grew within mudstone-dominated host rock in accordance with the
529 same diagenetic mechanism as the one typically associated with polygonal faults (Figure 1C)
530 (Ghalayini et al., 2017; Ghalayini and Eid, 2020). Based on their relative geographic proximity,
531 and the geometrical similarities between the piano-key faults in the Northern and Southern
532 Levant Basins, we here test the role of such proposed diagenetic model in the latter.

533 Despite having nucleated in a mudstone dominated Unit 7, our lithological analysis shows the
534 layer-bound faults in our study area had propagated through a ~2 km thick sandstone-
535 dominated host rock, challenging the application of the diagenetic model for the Southern
536 Levant Basin. Our interpretation is that nucleation and growth were not triggered by near-
537 surface diagenesis of fine-grained sediments, as supported by our kinematic analysis.

538 Assuming the depth of maximum throw corresponds to the depth of fault nucleation (Nicol et
539 al., 1996b; Kim and Sanderson, 2005), the dominant maximum throw along the Intra-
540 Burdigalian implies that all the faults types in our study area nucleated along the Intra-
541 Burdigalian horizon (17.54 Ma). As the Intra-Burdigalian horizons defines the base of the fault-
542 related growth strata (i.e., Unit 7), we can infer the faults nucleated as syn-depositional faults,
543 displacing the seabed, during the Late Burdigalian. Thus, our throw-depth plots (e.g., Figure
544 12) and interval thickness maps (Figure 5) suggest that the nucleation site of the layer-bound
545 faults mapped in our dataset was located at the top of the fault surface, with significant down-
546 dip fault propagation responsible for their vertical height. This observation does not match

547 most true polygonal fault throw profiles, where the nucleation site is located either at their
548 centre or base of the fault surface (Cartwright, 2011; Wrona et al., 2017). Such an apparent
549 discrepancy can allude to a difference in the mechanical model responsible for fault nucleation
550 and subsequent growth. Whereas true polygonal faults must first be buried to activate the
551 diagenetic processes, the layer-bound faults in our study area had nucleated as syn-depositional
552 faults close to the seabed and propagated downwards. Second, the current distribution of strain
553 in the fault system studied here is more interconnected and thus matures at relatively shallow
554 depths, in contrast to true polygonal fault systems that display an increasing number of hard
555 linkages downwards (Cartwright, 2011; Seebeck et al., 2015) (Figure 11).

556 Therefore, based on the abundance of sand-dominated units the faults had to propagate, and
557 the abnormal throw-distribution compared to “true” polygonal faults along the fault plane, we
558 suggest that the layer-bound faults in our study area did not form by the same diagenetic
559 mechanism as true polygonal faults; bringing us to an alternative, tectonic-related model (see
560 Sub-Section 6.1.2.).

561 *6.1.2. Tectonically induced layer-bound faulting*

562 Given our arguments against a diagenetic model for fault development, we here present an
563 alternative model that is summarised in Figure 14. Our model uses our age-constrained seismic-
564 stratigraphic framework and refers to the tectono-stratigraphic events that shaped the basin
565 during times of fault nucleation and subsequent growth.

566 First, we note that Unit 2 acts as a basal décollement layer for the layer-bound faults across not
567 only the Southern Levant Basin, as demonstrated here, but across much of the eastern
568 Mediterranean (Hawie et al., 2013; Ghalayini et al., 2014, 2017; Gao et al., 2020). To the best
569 of our knowledge, X-1 is the only well in the basin to penetrate Unit 2. This well encountered
570 Late Eocene strata but was aborted due to overpressure at that level. The exact reason for this
571 overpressure is not known, but it is possible that the overpressure was developed by the rapidly
572 buried Unit 2, leading to trapped fluids in the chalk and marls, eventually creating favourable
573 conditions for overpressure to build. From a geodynamic perspective, compressional stresses
574 associated with Syrian Arc folding, which were highest during the Senonian - Eocene, are
575 thought to have declined during the Oligocene (Sagy et al., 2018). This decrease in tectonic
576 deformation is recorded in our study by a broadly isopachous, Early Oligocene unit (i.e., Unit
577 3) (Figure 5 and 14A). Rapid deposition continued throughout the Oligocene and Early
578 Miocene (i.e., Units 4 and 5). This could therefore have caused pore pressure to build in the

579 now-buried chalk and marls, raising the vertical confining stress σ_v and eventually forming a
580 décollement (Figure 14 B&C).

581 Following this period of tectonic quiescence since Eocene, evidence for deformation appear
582 again in the Burdigalian. Thinning of the sandstone-dominated, Lower Burdigalian (Unit 6)
583 towards the WSW-ENE-striking strike-slip fault, suggest this large fault was active at this time
584 (Figure 5E). Initial activation of this strike-slip fault was followed by intense layer-bound
585 faulting during the Late Burdigalian, in the mudstone-dominated Unit 7a (Figure 8E and 14D).
586 By the end of the Langhian, both the strike-slip movement and the layer-bound normal faulting
587 had stopped, while uplift of the Leviathan High became the most prominent deformation event
588 (Figure 8D). The nucleation and subsequent growth of the faults prior to the culmination of any
589 large-scale uplift, allows us to disregard the folding of the Leviathan High as a mechanism for
590 the development of the normal faults.

591 We do note however, an apparent kinematic relationship between the WSW-ENE-striking
592 strike-slip fault, and the layer-bound normal faulting, as both faulting systems were most active
593 during the Late Burdigalian and had mostly ceased by the end of the Langhian. The origin of
594 this strike-slip faulting is beyond the scope of this manuscript. However, we do highlight
595 several significant geodynamic events that occurred in and around the basin during times of
596 fault activation: (1) a landward jump of strain from the Continental Fault Zone along the Levant
597 eastern margin, to the sinistral movement along the Dead Sea transform (Gvirtzman and
598 Steinberg, 2012; Nuriel et al., 2017); (2) the development of the Dead Sea transform (Freund
599 et al., 1968; Segev et al., 2014; Nuriel et al., 2017); (3) the final closure of the Indian Ocean-
600 Mediterranean Seaway (Bialik et al., 2019; Torfstein and Steinberg, 2020); (4) change in the
601 subduction rates and slab angle beneath the Cyprus Arc subduction zone (Gao et al., 2020;
602 Aksu et al., 2021) (5) uplift of the Eratosthenes Seamount by >1 km at the Early Miocene
603 (Robertson, 1998b; Papadimitriou et al., 2018; Gao et al., 2020)

604 A geodynamic outcome of these tectonic events may have been a counter clockwise rotation
605 of the basin, created by the non-subsiding Eratosthenes Seamount (Robertson, 2007;
606 Papadimitriou et al., 2018; Aksu et al., 2021) (Figure 14E). As the Eratosthenes Seamount was
607 stuck in place, the Levant Basin and its onshore segments, which continued to move
608 northwards, rotated counter clockwise around Eratosthenes. This counter-clockwise rotation
609 could have therefore caused the formation of the offshore dextral strike-slip faults found in our
610 dataset and offshore Lebanon (Figure 14E). A similar interpretation is made by Ghalayini et

611 al. (2014), with these authors suggesting that continued sinistral movement along the Levant
612 Fracture System onshore Lebanon caused (dextral) strike-slip reactivation of Cenozoic, rift-
613 related normal faults. They then propose that the relative movement along the strike-slip faults
614 eventually created onshore counter-clockwise block rotation, absorbing any extension in the
615 Levant Fracture System pull-up structures onshore Lebanon.

616 We here build on the model of Ghalayini et al. (2014) and propose that thick-skinned, dextral
617 strike-slip movement along WSW-ENE-striking strike-slip faults occurred in response to the
618 large-scale, geodynamic reorganisation of the Levant Basin. This strike-slip movement induced
619 local extensional stresses and strain, with one expression of this being the NW-SE-striking,
620 layer-bound normal faults (Figure 14). After nucleating, the NW-SE-striking faults propagated
621 through the Oligocene-Miocene units until their lower tips decoupled within the overpressured
622 Senonian - Eocene unit. By introducing this tectonic-driven model we can explain: (1) the
623 direct kinematic relationship we presented between the WSW-ENE-striking strike-slip fault
624 and the NW-SE-striking faults; (2) the change in orientation from NW-SE-striking to a more
625 E-W-striking, riedel-like orientation close to the strike-slip faults, as observed here and
626 offshore Lebanon; (3) how the NW-SE-striking, layer-bound faults propagated through a ~ 2
627 km-thick sandstone-dominated unit; (4) why the faults are so linear, and strike almost
628 perpendicular to the current basin margin.

629 We do note that, unlike the Eocene, which is the lower boundary for the entire fault system
630 across the Levant basin, the faults upper boundary varies; from the base-Evaporite (5.96 Ma)
631 unit in the Northern Levant Basin, to the Top Langhian (13.84 Ma) at the Southern Levant
632 Basin. We do not have clear explanation to this discrepancy. One possibility is that the strike-
633 slip faults, and their kinematically related normal faults, remained active for longer in the
634 Northern Levant Basin (Ghalayini et al., 2014). Another possibility for this discrepancy is the
635 presence of the chaotic section in Unit 9 in our dataset, which is not present in the Northern
636 Levant Basin. It is therefore possible that upper fault propagation was inhibited by the more
637 ductile nature of the chaotic section.

638 **7. Conclusions**

639 We use high-quality 3D seismic reflection, biostratigraphy, and well-log data to characterise
640 the spatial and temporal evolution of a layer-bound fault system in the Southern Levant Basin,
641 offshore Israel. We present a new, age-constrained, pre-Messinian seismic-stratigraphic
642 framework for the basin, discussing the lithological variability and prominent thickness

643 changes occurring within key intervals. This seismic-stratigraphic framework allows us to
644 describe the prominent structural elements in our study area, which include the NW-striking,
645 layer-bound faults, the triangular Leviathan High, and a prominent, WSW-striking, dextral
646 strike-slip fault. Throw-depth profiles, expansion index, and thickness changes all indicate the
647 layer-bound faults nucleated as syn-depositional faults during the Late Burdigalian (~15-17.54
648 Ma) in a mudstone-dominated unit. The faults then propagated downwards through sandstone-
649 dominated Oligocene-Miocene units, tipping-out within an overpressured Eocene-Senonian
650 strata. The NW-striking faults also appear to be kinematically linked to the WSW-striking
651 strike-slip.

652 Based on: (1) their direct kinematic relations to the strike-slip fault; (2) their propagation
653 through sandstone-dominated strata; (3) throw-depth profiles which show maximum throw at
654 the top of the faults, differing from other documented polygonal faults; and despite nucleating
655 in a mudstone-dominated unit, we suggest the faults did not develop through a diagenetic
656 process as previously suggested, but as a thin-skinned response to a thick-skinned tectonic
657 reorganisation of the basin. The precise mechanics and kinematics of this geodynamic events
658 are not clear, but they may relate to a possible counter-clockwise rotation of the basin, with
659 spatially limited extension being accommodated by the layer-bound faults. This model suggests
660 that basin-scale layer-bound normal faults can develop not only through a diagenetic model as
661 proposed for polygonal faults, but also by tectonic-related processes. Therefore, we suggest
662 that linear, layer-bound normal fault system should be investigated in the context of the basin
663 in which they formed in.

664 **References**

- 665 Aksu, A. E., J. Hall, and C. Yaltrak, 2021, Miocene–Quaternary tectonic, kinematic and
666 sedimentary evolution of the eastern Mediterranean Sea: A regional synthesis: *Earth-*
667 *Science Reviews*, v. 220, p. 103719, doi:<https://doi.org/10.1016/j.earscirev.2021.103719>.
- 668 Bar, O., Z. Gvirtzman, S. Feinstein, and E. Zilberman, 2013, Accelerated subsidence and
669 sedimentation in the Levant Basin during the Late Tertiary and concurrent uplift of the
670 Arabian platform: Tectonic versus counteracting sedimentary loading effects: *Tectonics*,
671 v. 32, no. 3, p. 334–350, doi:[10.1002/tect.20026](https://doi.org/10.1002/tect.20026).

672 Bar, O., E. Zilberman, S. Feinstein, R. Calvo, and Z. Gvirtzman, 2016, The uplift history of the
673 Arabian Plateau as inferred from geomorphologic analysis of its northwestern edge:
674 *Tectonophysics*, v. 671, p. 9–23, doi:10.1016/j.tecto.2016.01.004.

675 Barnett, J. A. M., J. Mortimer, J. H. Rippon, J. J. Walsh, and J. Watterson, 1987, Displacement
676 Geometry in the Volume Containing a Single Normal Fault1: *AAPG Bulletin*, v. 71, no.
677 8, p. 925–937, doi:10.1306/948878ED-1704-11D7-8645000102C1865D.

678 Baudon, C., and J. Cartwright, 2008, The kinematics of reactivation of normal faults using high
679 resolution throw mapping: *Journal of Structural Geology*, v. 30, no. 8, p. 1072–1084,
680 doi:10.1016/j.jsg.2008.04.008.

681 Ben-Gai, Y., 2018, The Leviathan Miocene Diapir – A novel insight into the tectonic evolution
682 of the Southern Levant Basin, Eastern Mediterranean: *Marine and Petroleum Geology*, v.
683 89, p. 701–713, doi:10.1016/j.marpetgeo.2017.11.002.

684 Bialik, O. M., M. Frank, C. Betzler, R. Zammit, and N. D. Waldmann, 2019, Two-step closure
685 of the Miocene Indian Ocean Gateway to the Mediterranean: *Scientific Reports*, v. 9, no.
686 1, p. 1–10, doi:10.1038/s41598-019-45308-7.

687 Bosworth, W., P. Huchon, and K. McClay, 2005, The Red Sea and Gulf of Aden Basins:
688 *Journal of African Earth Sciences*, v. 43, no. 1, p. 334–378,
689 doi:https://doi.org/10.1016/j.jafrearsci.2005.07.020.

690 Bosworth, W., D. F. Stockli, and D. E. Helgeson, 2015, Integrated outcrop, 3D seismic, and
691 geochronologic interpretation of Red Sea dike-related deformation in the Western Desert,
692 Egypt – The role of the 23Ma Cairo “mini-plume”: *Journal of African Earth Sciences*, v.
693 109, p. 107–119, doi:https://doi.org/10.1016/j.jafrearsci.2015.05.005.

694 Carruthers, D., J. Cartwright, M. P. A. Jackson, and P. Schutjens, 2013, Origin and timing of
695 layer-bound radial faulting around north sea salt stocks: New insights into the evolving
696 stress state around rising diapirs: *Marine and Petroleum Geology*, v. 48, p. 130–148,
697 doi:10.1016/j.marpetgeo.2013.08.001.

698 Cartwright, J., 2011, Diagenetically induced shear failure of fine-grained sediments and the
699 development of polygonal fault systems: *Marine and Petroleum Geology*, v. 28, no. 9, p.
700 1593–1610, doi:10.1016/J.MARPETGEO.2011.06.004.

- 701 Cartwright, J., R. Bouroullec, D. James, and H. Johnson, 1998, Polycyclic motion history of
702 some Gulf Coast growth faults from high-resolution displacement analysis: *Geology*, v.
703 26, no. 9, p. 819–822, doi:10.1130/0091-7613(1998)026<0819:PMHOSG>2.3.CO;2.
- 704 Cartwright, J. A., and D. N. Dewhurst, 1998, Layer-bound compaction faults in fine-grained
705 sediments: *GSA Bulletin*, v. 110, no. 10, p. 1242–1257, doi:10.1130/0016-
706 7606(1998)110<1242:lbcfif>2.3.co;2.
- 707 Cartwright, J., D. James, and A. Bolton, 2003, The genesis of polygonal fault systems: A
708 review: *Geological Society Special Publication*, v. 216, p. 223–234,
709 doi:10.1144/GSL.SP.2003.216.01.15.
- 710 Cartwright, J. A., and L. Lonergan, 1996, Volumetric contraction during the compaction of
711 mudrocks: a mechanism for the development of regional-scale polygonal fault systems:
712 *Basin Research*, v. 8, no. 2, p. 183–193, doi:10.1046/j.1365-2117.1996.01536.x.
- 713 Childs, C., A. Nicol, J. J. Walsh, and J. Watterson, 1996, Growth of vertically segmented
714 normal faults: *Journal of Structural Geology*, v. 18, no. 12, p. 1389–1397,
715 doi:10.1016/S0191-8141(96)00060-0.
- 716 Childs, C., J. Watterson, and J. J. Walsh, 1995, Fault overlap zones within developing normal
717 fault systems: *Journal of the Geological Society*, v. 152, no. 3, p. 535 LP – 549,
718 doi:10.1144/gsjgs.152.3.0535.
- 719 Childs, C., R. P. Worthington, J. J. Walsh, and V. Roche, 2019, Conjugate relay zones:
720 geometry of displacement transfer between opposed-dipping normal faults: *Journal of*
721 *Structural Geology*, v. 118, p. 377–390, doi:https://doi.org/10.1016/j.jsg.2018.11.007.
- 722 Christensen, C. J., and G. Powers, 2013, Formation Evaluation Challenges In Tamar Field,
723 Offshore Israel, *in* SPWLA 54th Annual Logging Symposium: p. 1–12.
- 724 Cohen, Z., V. Kaptan, and A. Flexer, 1990, The Tectonic Mosaic of the Southern Levant:
725 implications for Hydrocarbon Prospects: *Journal of Petroleum Geology*, v. 13, no. 4, p.
726 437–462, doi:10.1111/j.1747-5457.1990.tb00858.x.
- 727 Craik, D., and Y. Ben-Gai, 2019, Syn-Tectonic Sedimentation Over a Miocene Gas-Bearing
728 Structure-Sequence Stratigraphy Case Study of the Aphrodite Field, Levant Basin*:
729 *Search and Discovery*, doi:10.1306/20464Craik2019.

- 730 Dawers, N. H., and M. H. Anders, 1995, Displacement-length scaling and fault linkage: Journal
731 of Structural Geology, v. 17, no. 5, p. 607–614, doi:[https://doi.org/10.1016/0191-](https://doi.org/10.1016/0191-8141(94)00091-D)
732 8141(94)00091-D.
- 733 Dewhurst, D. N., J. A. Cartwright, and L. Lonergan, 1999, The development of polygonal fault
734 systems by syneresis of colloidal sediments: Marine and Petroleum Geology, v. 16, no. 8,
735 p. 793–810, doi:10.1016/S0264-8172(99)00035-5.
- 736 Druckman, Y., 1994, Subsurface geology and structural evolution of the northwestern Negev,
737 southern Israel: Geological Survey of Israel.
- 738 Eckersley, A. J., J. Lowell, and P. Szafian, 2018, High-definition frequency decomposition:
739 Geophysical Prospecting, v. 66, no. 6, p. 1138–1143, doi:[https://doi.org/10.1111/1365-](https://doi.org/10.1111/1365-2478.12642)
740 2478.12642.
- 741 Eyal, Y., 1996, Stress field fluctuations along the Dead Sea rift since the middle Miocene:
742 Tectonics, v. 15, no. 1, p. 157–170, doi:10.1029/95TC02619.
- 743 Faccenna, C., P. Glišović, A. Forte, T. W. Becker, E. Garzanti, A. Sembroni, and Z. Gvirtzman,
744 2019, Role of dynamic topography in sustaining the Nile River over 30 million years:
745 Nature Geoscience, v. 12, no. 12, p. 1012–1017, doi:10.1038/s41561-019-0472-x.
- 746 Freund, R., 1975, The Triassic-Jurassic structure of Israel and its relation to the origin of the
747 eastern Mediterranean: Geological Survey of Israel.
- 748 Freund, R., I. Zak, and Z. W. I. Garfunkel, 1968, Age and rate of the sinistral movement along
749 the Dead Sea Rift: Nature, v. 220, no. 5164, p. 253–255.
- 750 Gao, H., Z. Wen, B. Shi, Z. Wang, and C. Song, 2020, Tectonic characteristics of the t and its
751 periphery: Implications for evolution of the eastern Mediterranean: Marine Geology, v.
752 428, p. 106266, doi:<https://doi.org/10.1016/j.margeo.2020.106266>.
- 753 Gardosh, M. A., and Y. Druckman, 2006, Seismic stratigraphy, structure and tectonic evolution
754 of the Levantine Basin, offshore Israel: Geological Society Special Publication, v. 260,
755 no. 1, p. 201–227, doi:10.1144/GSL.SP.2006.260.01.09.
- 756 Gardosh, M., Y. Druckman, B. Buchbinder, and R. Calvo, 2008, The Oligo-Miocene deepwater
757 system of the Levant Basin: Geological Survey of Israel, 73 p., doi:GSI/33/2008.

- 758 Gardosh, M., Y. Druckman, B. Buchbinder, and M. Rybakov, 2008, The Levant Basin Offshore
759 Israel: Stratigraphy, Structure, Tectonic Evolution and Implications for Hydrocarbon
760 Exploration - revised edition. Geological Survey of Israel report GSI/4/2008: Geological
761 Survey of Israel, 121 p.
- 762 Gardosh, M., Z. Garfunkel, Y. Druckman, and B. Buchbinder, 2010, Tethyan rifting in the
763 Levant Region and its role in Early Mesozoic crustal evolution: Geological Society,
764 London, Special Publications, v. 341, no. 1, p. 9 LP – 36, doi:10.1144/SP341.2.
- 765 Gardosh, M. A., and E. Tannenbaum, 2014, The Petroleum Systems of Israel, *in* Memoir 106:
766 Petroleum Systems of the Tethyan Region: AAPG Special Volumes, p. 179–216,
767 doi:10.1306/13431857m106298.
- 768 Gardosh, M., P. Weimer, and A. Flexer, 2011, The sequence stratigraphy of Mesozoic
769 successions in the Levant margin, southwestern Israel: A model for the evolution of
770 southern Tethys margins: AAPG Bulletin, v. 95, no. 10, p. 1763–1794,
771 doi:10.1306/02081109135.
- 772 Garfunkel, Z., 1998, Constrains on the origin and history of the Eastern Mediterranean basin:
773 Tectonophysics, v. 298, no. 1–3, p. 5–35, doi:10.1016/S0040-1951(98)00176-0.
- 774 Garfunkel, Z., 1981, Internal structure of the Dead Sea leaky transform (rift) in relation to plate
775 kinematics: Tectonophysics, v. 80, no. 1–4, p. 81–108, doi:10.1016/0040-1951(81)90143-
776 8.
- 777 Garfunkel, Z., 2004, Origin of the Eastern Mediterranean basin: A reevaluation:
778 Tectonophysics, v. 391, no. 1- 4 SPEC.ISS., p. 11–34, doi:10.1016/j.tecto.2004.07.006.
- 779 Garfunkel, Z., 1997, The history and formation of the Dead Sea basin, *in* T. M. Niemi, Z. Ben-
780 Avraham, and J. R. Gat, eds., The Dead Sea, the Lake and its Setting: Oxford University
781 Press, USA, p. 36–56.
- 782 Garfunkel, Z., and B. Derin, 1984, Permian-early Mesozoic tectonism and continental margin
783 formation in Israel and its implications for the history of the Eastern Mediterranean:
784 Geological Society Special Publication, v. 17, no. 1, p. 187–201,
785 doi:10.1144/GSL.SP.1984.017.01.12.

- 786 Ghalayini, R., J.-M. Daniel, C. Homberg, F. H. Nader, and J. E. Comstock, 2014, Impact of
787 Cenozoic strike-slip tectonics on the evolution of the northern Levant Basin (offshore
788 Lebanon): *Tectonics*, v. 33, no. 11, p. 2121–2142, doi:10.1002/2014TC003574.
- 789 Ghalayini, R., and C. Eid, 2020, Using polygonal layer-bound faults as tools to delimit clastic
790 reservoirs in the Levant Basin offshore Lebanon: *AAPG Bulletin*, v. 104, no. 3, p. 629–
791 656, doi:10.1306/07151918155.
- 792 Ghalayini, R., C. Homberg, J. M. Daniel, and F. H. Nader, 2017, Growth of layer-bound normal
793 faults under a regional anisotropic stress field: Geological Society, London, Special
794 Publications, v. 439, no. 1, p. 57 LP – 78, doi:10.1144/SP439.13.
- 795 Gouliotis, L., 2019, Tectonic Structure of the Karish Gas Field, Offshore Israel *Tectonics and*
796 *Hydrogeology of Sterea Hellas View project Researches on the geology of Greece View*
797 *project: Search and Discovery*, no. 30638, doi:10.1306/30638Gouliotis2019.
- 798 Goult, N. R., 2008, Geomechanics of polygonal fault systems: A review: p. 389–397,
799 doi:10.1144/1354-079308-781.
- 800 Goult, N. R., 2002, Mechanics of layer-bound polygonal faulting in fine-grained sediments:
801 *Journal of the Geological Society*, v. 159, no. 3, p. 239–246, doi:10.1144/0016-764901-
802 111.
- 803 Granot, R., 2016, Palaeozoic oceanic crust preserved beneath the eastern Mediterranean:
804 *Nature Geoscience*, v. 9, no. 9, p. 701–705, doi:10.1038/ngeo2784.
- 805 Gvirtzman, Z., I. Csato, and D. Granjeon, 2014, Constraining sediment transport to deep marine
806 basins through submarine channels: The Levant margin in the Late Cenozoic: *Marine*
807 *Geology*, v. 347, p. 12–26, doi:10.1016/j.margeo.2013.10.010.
- 808 Gvirtzman, Z., M. Reshef, O. Buch-Leviatan, G. Groves-Gidney, Z. Karcz, Y. Makovsky, and
809 Z. Ben-Avraham, 2015, Bathymetry of the Levant basin: Interaction of salt-tectonics and
810 surficial mass movements: *Marine Geology*, v. 360, p. 25–39,
811 doi:10.1016/j.margeo.2014.12.001.
- 812 Gvirtzman, Z., and J. Steinberg, 2012, Inland jump of the Arabian northwest plate boundary
813 from the Levant continental margin to the Dead Sea Transform: *Tectonics*, v. 31, no. 4, p.
814 n/a-n/a, doi:10.1029/2011TC002994.

815 Gvirtzman, Z., J. Steinberg, O. Bar, B. Buchbinder, E. Zilberman, R. Siman-Tov, R. Calvo, L.
816 Grossowicz, A. Almogi-Labin, and M. Rosensaft, 2011, Retreating late tertiary shorelines
817 in Israel: Implications for the exposure of north Arabia and levant during Neotethys
818 closure: *Lithosphere*, v. 3, no. 2, p. 95–109, doi:10.1130/L124.1.

819 Hawie, N., C. Gorini, R. Deschamps, F. H. Nader, L. Montadert, D. Granjeon, and F. Baudin,
820 2013, Tectono-stratigraphic evolution of the northern Levant Basin (offshore Lebanon):
821 *Marine and Petroleum Geology*, v. 48, p. 392–410, doi:10.1016/j.marpetgeo.2013.08.004.

822 Hsü, K. J., L. Montadert, D. Bernoulli, M. B. Cita, A. Erickson, R. E. Garrison, R. B. Kidd, F.
823 Mèlières, C. Müller, and R. Wright, 1977, History of the mediterranean salinity crisis:
824 *Nature*, v. 267, no. 5610, p. 399–403, doi:10.1038/267399a0.

825 Ireland, M. T., N. R. Goult, and R. J. Davies, 2011, Influence of stratigraphic setting and
826 simple shear on layer-bound compaction faults offshore Mauritania: *Journal of Structural*
827 *Geology*, v. 33, no. 4, p. 487–499, doi:10.1016/j.jsg.2010.11.005.

828 Jackson, C. A. L., R. E. Bell, A. Rotevatn, and A. B. M. Tvedt, 2017, Techniques to determine
829 the kinematics of synsedimentary normal faults and implications for fault growth models:
830 *Geological Society Special Publication*, v. 439, no. 1, p. 187–217, doi:10.1144/SP439.22.

831 Jackson, C. A. L., D. T. Carruthers, S. N. Mahlo, and O. Briggs, 2014, Can polygonal faults
832 help locate deep-water reservoirs? *AAPG Bulletin*, v. 98, no. 9, p. 1717–1738,
833 doi:10.1306/03131413104.

834 Jackson, C. A. L., and A. Rotevatn, 2013, 3D seismic analysis of the structure and evolution
835 of a salt-influenced normal fault zone: A test of competing fault growth models: *Journal*
836 *of Structural Geology*, v. 54, p. 215–234, doi:10.1016/j.jsg.2013.06.012.

837 Kanari, M., G. Tibor, J. K. Hall, T. Ketter, G. Lang, and U. Schattner, 2020, Sediment transport
838 mechanisms revealed by quantitative analyses of seafloor morphology: New evidence
839 from multibeam bathymetry of the Israel exclusive economic zone: *Marine and Petroleum*
840 *Geology*, v. 114, p. 104224, doi:10.1016/j.marpetgeo.2020.104224.

841 Karcz, K., Y. Gellman, O. Shitrit, and J. Steinberg, 2019, The Leviathan Field - Nine Years
842 Since Discovery and Nearing First Gas, *in* Second EAGE Eastern Mediterranean
843 Workshop: European Association of Geoscientists & Engineers, p. 1–5,
844 doi:10.3997/2214-4609.201903152.

845 Kim, Y. S., and D. J. Sanderson, 2005, The relationship between displacement and length of
846 faults: A review: *Earth-Science Reviews*, v. 68, no. 3–4, p. 317–334,
847 doi:10.1016/j.earscirev.2004.06.003.

848 King, J. J., and J. Cartwright, 2020, Ultra-slow throw rates of polygonal fault systems:
849 Geological Society of America | *GEOLOGY*, v. 48, p. 473–477, doi:10.1130/G47221.1.

850 Kosi, W., G. Tari, F. H. Nader, C. Skiple, B. Trudgill, and D. Lazar, 2012, Structural analogy
851 between the “piano key faults” of deep-water Lebanon and the extensional faults of the
852 Canyonlands grabens, Utah, United States: *The Leading Edge*, v. 31, no. 7, p. 824–830,
853 doi:10.1190/tle31070824.1.

854 Krenkel, E., 1924, Der Syrische Bogen: *Zentralblatt Mineralogie*, v. 9, no. 10, p. 274–281.

855 Krijgsman, W., F. J. Hilgen, I. Raffi, F. J. Sierro, and D. S. Wilson, 1999, Chronology, causes
856 and progression of the Messinian salinity crisis: *Nature*, v. 400, no. 6745, p. 652–655,
857 doi:10.1038/23231.

858 Lathrop, B., C. A. L. Jackson, and A. Rotevatn, n.d., Normal Fault Database_Lathrop.xlsx:
859 <https://figshare.com/articles/dataset/Normal_Fault_Database_Lathrop_xlsx/17087273>
860 (accessed February 23, 2022).

861 Lonergan, L., J. Cartwright, and R. Jolly, 1998, The geometry of polygonal fault systems in
862 Tertiary mudrocks of the North Sea: *Journal of Structural Geology*, v. 20, no. 5, p. 529–
863 548, doi:10.1016/S0191-8141(97)00113-2.

864 Morag, N., I. Haviv, and Y. Katzir, 2016, From ocean depths to mountain tops: Uplift of the
865 Troodos ophiolite (Cyprus) constrained by low-temperature thermochronology and
866 geomorphic analysis: *Tectonics*, v. 35, no. 3, p. 622–637, doi:10.1002/2015TC004069.

867 Morgan, D. A., J. A. Cartwright, and P. Imbert, 2015, Perturbation of polygonal fault
868 propagation by buried pockmarks and the implications for the development of polygonal
869 fault systems: *Marine and Petroleum Geology*, v. 65, p. 157–171,
870 doi:10.1016/j.marpetgeo.2015.03.024.

871 Muraoka, H., and H. Kamata, 1983, Displacement distribution along minor fault traces: *Journal*
872 *of Structural Geology*, v. 5, no. 5, p. 483–495, doi:10.1016/0191-8141(83)90054-8.

873 Needham, D. L., H. S. Pettingill, C. J. Christensen, J. Ffrench, and Z. K. Karcz, 2017, The
874 Tamar giant gas field: Opening the Subsalt Miocene gas play in the Levant Basin, *in*

875 AAPG Memoir: American Association of Petroleum Geologists, p. 221–256,
876 doi:10.1306/13572009M1133688.

877 Nicol, A., J. J. Walsh, P. Villamor, H. Seebeck, and K. R. Berryman, 2010, Normal fault
878 interactions, paleoearthquakes and growth in an active rift: *Journal of Structural Geology*,
879 v. 32, no. 8, p. 1101–1113, doi:<https://doi.org/10.1016/j.jsg.2010.06.018>.

880 Nicol, A., J. Watterson, J. J. Walsh, and C. Childs, 1996a, The shapes, major axis orientations
881 and displacement patterns of fault surfaces: *Journal of Structural Geology*, v. 18, no. 2, p.
882 235–248, doi:[https://doi.org/10.1016/S0191-8141\(96\)80047-2](https://doi.org/10.1016/S0191-8141(96)80047-2).

883 Nicol, A., J. Watterson, J. J. Walsh, and C. Childs, 1996b, The shapes, major axis orientations
884 and displacement patterns of fault surfaces: *Journal of Structural Geology*, v. 18, no. 2, p.
885 235–248, doi:[https://doi.org/10.1016/S0191-8141\(96\)80047-2](https://doi.org/10.1016/S0191-8141(96)80047-2).

886 Nuriel, P., R. Weinberger, A. R. C. Kylander-Clark, B. R. Hacker, and J. P. Craddock, 2017,
887 The onset of the Dead Sea transform based on calcite age-strain analyses: *Geology*, v. 45,
888 no. 7, p. 587–590, doi:10.1130/G38903.1.

889 Ortega, J., R. Hebert, and Y. Gellman, 2019, The Dynamic Tamar Reservoir: Insights from
890 Five Years of Production*: *Search and Discovery*, doi:10.1306/20465Ortega2019.

891 Papadimitriou, N., C. Gorini, F. H. Nader, R. Deschamps, V. Symeou, and J. C. Lecomte, 2018,
892 Tectono-stratigraphic evolution of the western margin of the Levant Basin (offshore
893 Cyprus): *Marine and Petroleum Geology*, v. 91, p. 683–705,
894 doi:10.1016/j.marpetgeo.2018.02.006.

895 Peacock, D. C. P., and D. J. Sanderson, 1991, Displacements, segment linkage and relay ramps
896 in normal fault zones: *Journal of Structural Geology*, v. 13, no. 6, p. 721–733,
897 doi:[https://doi.org/10.1016/0191-8141\(91\)90033-F](https://doi.org/10.1016/0191-8141(91)90033-F).

898 Peacock, D. C. P., and D. J. Sanderson, 1996, Effects of propagation rate on displacement
899 variations along faults: *Journal of Structural Geology*, v. 18, no. 2–3, p. 311–320,
900 doi:10.1016/S0191-8141(96)80052-6.

901 Reiche, S., C. Hübscher, and M. Beitz, 2014, Fault-controlled evaporite deformation in the
902 Levant Basin, Eastern Mediterranean: *Marine Geology*, v. 354, p. 53–68,
903 doi:10.1016/j.margeo.2014.05.002.

- 904 Robertson, A., 1998a, Mesozoic-Tertiary tectonic evolution of the easternmost Mediterranean
905 area: Integration of marine and land evidence: Proceedings of the Ocean Drilling Program:
906 Scientific Results, v. 160, p. 723–784, doi:10.2973/odp.proc.sr.160.061.1998.
- 907 Robertson, A., 2007, Overview of tectonic settings related to the rifting and opening of
908 Mesozoic ocean basins in the Eastern Tethys: Oman, Himalayas and Eastern
909 Mediterranean regions: Geological Society of London, p. 325–388,
910 doi:10.1144/SP282.15.
- 911 Robertson, A., 1998b, Tectonic significance of the Eratosthenes Seamount: a continental
912 fragment in the process of collision with a subduction zone in the eastern Mediterranean
913 (Ocean Drilling Program Leg 160): Tectonophysics, v. 298, no. 1, p. 63–82,
914 doi:https://doi.org/10.1016/S0040-1951(98)00178-4.
- 915 Robson, A. G., R. C. King, and S. P. Holford, 2017, Structural evolution of a gravitationally
916 detached normal fault array: analysis of 3D seismic data from the Ceduna Sub-Basin,
917 Great Australian Bight: Basin Research, v. 29, no. 5, p. 605–624,
918 doi:https://doi.org/10.1111/bre.12191.
- 919 Roche, V., C. Homberg, and M. Rocher, 2012, Fault displacement profiles in multilayer
920 systems: From fault restriction to fault propagation: Terra Nova, v. 24, no. 6, p. 499–504,
921 doi:10.1111/j.1365-3121.2012.01088.x.
- 922 Rotevatn, A., C. A. L. Jackson, A. B. M. Tvedt, R. E. Bell, and I. Blækkan, 2019, How do
923 normal faults grow? Journal of Structural Geology, v. 125, p. 174–184,
924 doi:10.1016/j.jsg.2018.08.005.
- 925 Ryan, W. B. F., 2009, Decoding the mediterranean salinity crisis: Sedimentology, v. 56, no. 1,
926 p. 95–136, doi:10.1111/j.1365-3091.2008.01031.x.
- 927 Rykkelid, E., and H. Fossen, 2002, Layer rotation around vertical fault overlap zones:
928 observations from seismic data, field examples, and physical experiments: Marine and
929 Petroleum Geology, v. 19, no. 2, p. 181–192, doi:https://doi.org/10.1016/S0264-
930 8172(02)00007-7.
- 931 Sagy, Y., Z. Gvirtzman, and M. Reshef, 2018, 80 m.y. of folding migration: New perspective
932 on the Syrian arc from Levant Basin analysis: Geology, v. 46, no. 2, p. 175–178,
933 doi:10.1130/G39654.1.

- 934 Sagy, Y., Z. Gvirtzman, M. Reshef, and Y. Makovsky, 2015, The enigma of the Jonah high in
935 the middle of the Levant basin and its significance to the history of rifting:
936 *Tectonophysics*, v. 665, p. 186–198, doi:10.1016/j.tecto.2015.09.037.
- 937 Seebeck, H., E. Tenthorey, C. Consoli, and A. Nicol, 2015, Polygonal faulting and seal
938 integrity in the Bonaparte Basin, Australia: *Marine and Petroleum Geology*, v. 60, p. 120–
939 135, doi:10.1016/j.marpetgeo.2014.10.012.
- 940 Segev, A., V. Lyakhovsky, and R. Weinberger, 2014, Continental transform-rift interaction
941 adjacent to a continental margin: The Levant case study: Elsevier, p. 83–103,
942 doi:10.1016/j.earscirev.2014.08.015.
- 943 Stearman, M., B. Gergurich, T. Kent, A. Wickard, and F. Laugier, 2021, Miocene Deep-Water
944 Stratigraphic Architecture and Heterogeneity: Levant Basin, Offshore Cyprus and Israel,
945 *in* Third EAGE Eastern Mediterranean Workshop: European Association of Geoscientists
946 & Engineers, p. 1–3, doi:10.3997/2214-4609.202137034.
- 947 Steinberg, J., Z. Gvirtzman, Y. Folkman, and Z. Garfunkel, 2011, Origin and nature of the rapid
948 late Tertiary filling of the Levant Basin: *Geology*, v. 39, no. 4, p. 355–358,
949 doi:10.1130/G31615.1.
- 950 Steinberg, J., A. M. Roberts, N. J. Kusznir, K. Schafer, and Z. Karcz, 2018, Crustal structure
951 and post-rift evolution of the Levant Basin: *Marine and Petroleum Geology*, v. 96, p. 522–
952 543, doi:10.1016/j.marpetgeo.2018.05.006.
- 953 Stuevold, L. M., R. B. Faereth, L. Arnesen, J. Cartwright, and N. Möller, 2003, Polygonal
954 faults in the Ormen Lange Field, Møre Basin, offshore Mid Norway: Geological Society,
955 London, Special Publications, v. 216, no. 1, p. 263 LP – 281,
956 doi:10.1144/GSL.SP.2003.216.01.17.
- 957 Thorsen, C. E., 1963, Age of growth faulting in the southern Louisiana.: Gulf coast association
958 of geological societies, v. 13, p. 103–110.
- 959 Torfstein, A., and J. Steinberg, 2020, The Oligo–Miocene closure of the Tethys Ocean and
960 evolution of the proto-Mediterranean Sea: *Scientific Reports*, v. 10, no. 1, p. 13817,
961 doi:10.1038/s41598-020-70652-4.

- 962 Turrini, L., C. A.-L. Jackson, and P. Thompson, 2017, Seal rock deformation by polygonal
963 faulting, offshore Uruguay: *Marine and Petroleum Geology*, v. 86, p. 892–907,
964 doi:10.1016/j.marpetgeo.2017.06.038.
- 965 Tvedt, A. B. M., A. Rotevatn, C. A.-L. Jackson, H. Fossen, and R. L. Gawthorpe, 2013, Growth
966 of normal faults in multilayer sequences: A 3D seismic case study from the Egersund
967 Basin, Norwegian North Sea: *Journal of Structural Geology*, v. 55, p. 1–20,
968 doi:https://doi.org/10.1016/j.jsg.2013.08.002.
- 969 Walley, C. D., 1998, Some outstanding issues in the geology of Lebanon and their importance
970 in the tectonic evolution of the Levantine region: *Tectonophysics*, v. 298, no. 1–3, p. 37–
971 62, doi:10.1016/S0040-1951(98)00177-2.
- 972 Walsh, J. J., W. R. Bailey, C. Childs, A. Nicol, and C. G. Bonson, 2003, Formation of
973 segmented normal faults: a 3-D perspective: *Journal of Structural Geology*, v. 25, no. 8,
974 p. 1251–1262, doi:https://doi.org/10.1016/S0191-8141(02)00161-X.
- 975 Walsh, J. J., and J. Watterson, 1988, Analysis of the relationship between displacements and
976 dimensions of faults: *Journal of Structural Geology*, v. 10, no. 3, p. 239–247,
977 doi:10.1016/0191-8141(88)90057-0.
- 978 Walsh, J. J., and J. Watterson, 1990, New methods of fault projection for coalmine planning:
979 *Proceedings of the Yorkshire Geological Society*, v. 48, no. 2, p. 209 LP – 219,
980 doi:10.1144/pygs.48.2.209.
- 981 Wrona, T., C. Magee, C. A.-L. Jackson, M. Huuse, and K. G. Taylor, 2017, Kinematics of
982 Polygonal Fault Systems: Observations from the Northern North Sea: p. 101.
- 983 Zachos, J., M. Pagani, L. Sloan, E. Thomas, and K. Billups, 2001, Trends, Rhythms, and
984 Aberrations in Global Climate 65 Ma to Present: *Science*, v. 292, no. 5517, p. 686 LP –
985 693, doi:10.1126/science.1059412.
- 986 Ziegler, A. M., 2001, Late Permian to Holocene Paleofacies Evolution of the Arabian Plate and
987 its Hydrocarbon Occurrences: *GeoArabia*, v. 6, no. 3, p. 445–504.
- 988 Zucker, E., Z. Gvirtzman, J. Steinberg, and Y. Enzel, 2019, Salt tectonics in the Eastern
989 Mediterranean Sea: Where a giant delta meets a salt giant: *Geology*, v. 48, no. 2, p. 134–
990 138, doi:10.1130/g47031.1.
- 991

992 **Figure Captions**

993 Figure 1: (A) A regional map of the Levant basin. Zoomed area shows the Ghalayini and Eid,
994 (2020) published fault system offshore Lebanon and the three different fault types described
995 by them. (B) Throw-depth profiles of these three fault types described offshore Lebanon
996 (Modified from Ghalayini and Eid, 2020). (C) The diagenetically induced mechanical model
997 suggested by Ghalayini and Eid, (2020) for offshore Lebanon (A-C are modified from
998 Ghalayini and Eid, 2020).

999 Figure 2: (A) The location of the study area in the southern Levant basin, overlaid by the outline
1000 of our seismic data (white), the location of available wells (color coded) and the outline of the
1001 profile displayed in C. (B) The seismic-stratigraphic framework for the Southern Levant basin
1002 used in this study. (C) A depth migrated seismic cross-section through the available wells.
1003 Interpretation highlights the seismic-stratigraphic framework and the geometry of the piano-key
1004 layer bound faults.

1005 Figure 3: Lithological interpretation along the X-1 well. Integrating (from left to right) the
1006 seismic signature, GR log, sample cuttings, derived simplified lithology, and neutron-density
1007 log. The simplified lithology column represents the lithological variability of the faulted
1008 Oligocene – Miocene section. Depth axis in this and subsequent figures were removed
1009 according to the confidentiality agreements.

1010 Figure 4: Structural maps of the horizons used in the study, indicating the present-day geometry
1011 of the Oligocene-Miocene. Note the different depth ranges of the colour scales used for
1012 enhancing the structural elements in each map.

1013 Figure 5: Thickness maps of the seismic-stratigraphic units used in this study. Note the different
1014 thickness ranges of colour scales used for covering the entire thickness range of each unit. The
1015 maps indicate the study area had experience two main kinematic events. The first during the
1016 Eocene, where thinning is seen across the Leviathan High. This followed by a hiatus in tectonic
1017 events during Units 3-5 seen by an isopachous maps. The second kinematic event peaked in
1018 Unit 7, where thinning across the high, alongside across-fault thickening show faulting was
1019 associated with folding. Faulting had stopped in Unit 9, but folding seem to continue until the
1020 deposition of the Messinian evaporites.

1021 Figure 6: (A) Polygonal fabric mapped across the Top Langhian structural map. (B) A cross-
1022 section through this fabric. Black arrows indicate the local depressions which form this fabric

1023 along the Top Langhian horizon; (C) A zoomed part of the map in A showing the polygonal
1024 fabric becomes concentric around the adjacent Tamar anticline; (D) A zoomed part of the map
1025 in A showing most pronounced polygonal plan-form (white arrows); (E) A zoomed part of
1026 the map in C showing the NW-striking faults displace the polygonal fabric.

1027 Figure 7: Cross-section through two locations within the study area indicating growth-strata
1028 across the faults during the Late Burdigalian. Sections are located within (A), and away from
1029 the structural high (B), to indicate thickness changes occurred within Unit 7 regardless of the
1030 relative location to the structural high.

1031 Figure 8: Flattened on Top Langhian cross-section across the Leviathan structure (A), and two
1032 zoomed segments (B, C). These sections demonstrate overlapping surface within Unit 7 (dashed
1033 line) that is dated at 15 Ma (dotted line). (D) Thickness map of Unit 7b, i.e., Top Langhian
1034 (13.82 Ma) to overlapping surface (15 Ma). Folding related thickness changes are prominent,
1035 with very little faulting. (E) Thickness map of Unit 7a, i.e., Overlapping surface (15 Ma) to Intra-
1036 Burdigalian (17.54 Ma). Thickness changes show very intense faulting with little folding
1037 related thinning across the structure. White dotted lines show two WSW-ENE-striking faults
1038 with high intensity of faulting around them.

1039 Figure 9: A WSW-ENE-striking strike-slip fault. (A) An uninterpreted (left) and an interpreted
1040 (right) cross-section across the fault. A deep, singular, stem is affecting the entire sedimentary
1041 sequence in the basin with a negative flower structure developed in the younger units. (B) A
1042 thickness map of the Upper Langhian, showing thickening within the negative flower structure.
1043 (C) Left - Spectral decomposition along the Top Aquitanian horizon. Right - Simplified map
1044 of the faults along the Top Aquitanian. The maps indicate the WSW-ENE fault consists of
1045 three separate segments (marked as red faults), connected by the NW-striking faults in an en-
1046 echelon like arrangement (red arrows). Two more WSW-ENE-striking faults, located at the
1047 southern side of the Leviathan structure, are also highlighted in red arrows. The NW-striking
1048 faults are shorter, and with higher faulting intensity adjacent to the WSW-ENE faults. A dashed
1049 line represents the northern boundary of areas of bad imaging along the Top Aquitanian
1050 horizon.

1051 Figure 10: Geometrical properties of the faults. (A) Geographic location of the 136 mapped
1052 faults in the study area. Colours represent dip direction to the SW (red) and to the NE (blue)
1053 (B) Max throw vs fault length relative to the global database (Lathrop et al., in review). The
1054 faults are located within the global database and are not anomalous in that regard.

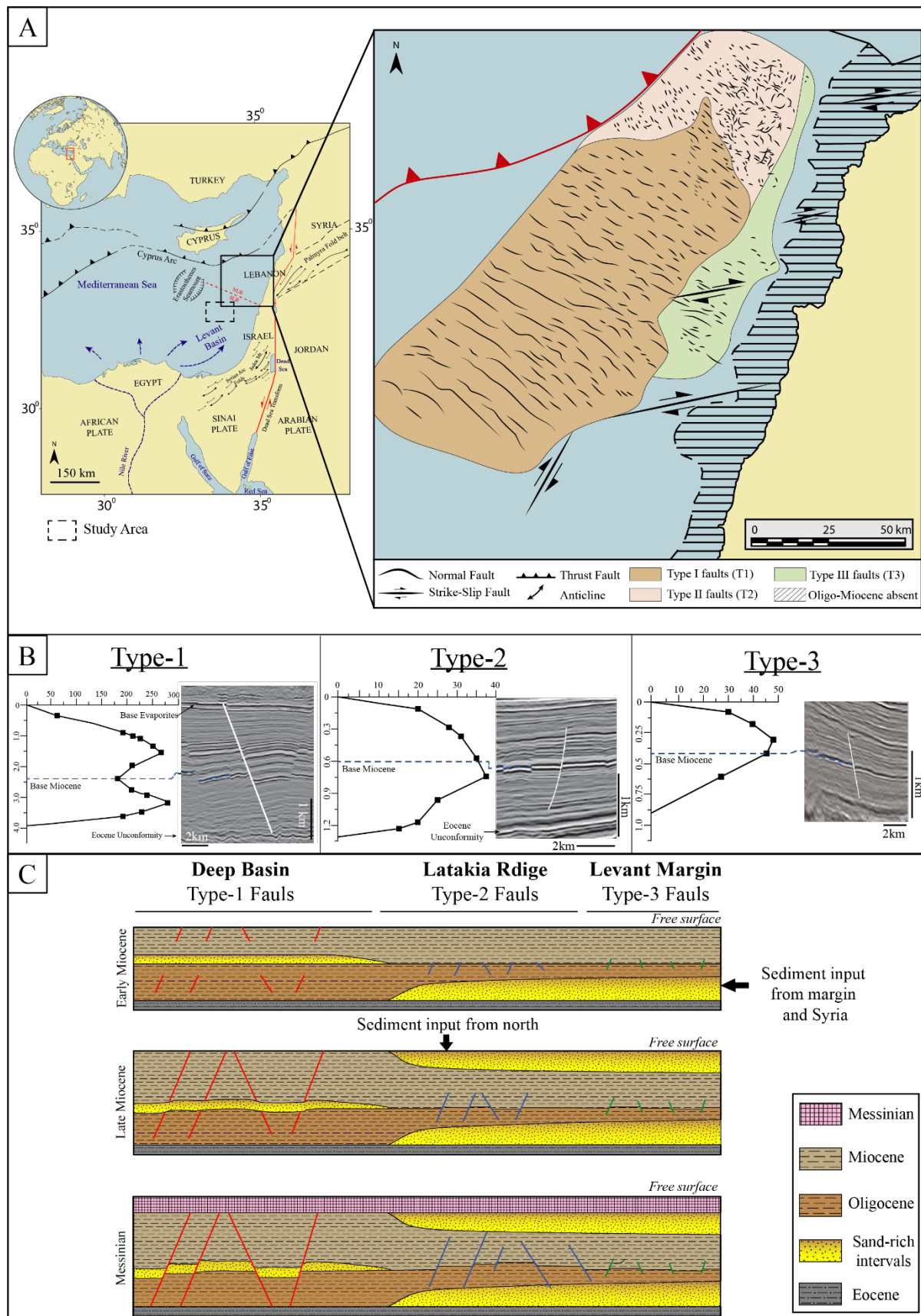
1055 Figure 11: Strike-parallel throw profiles of 120 faults along the top-most horizon (Top
1056 Langhian; top) and the base horizon (Base Oligocene; bottom) with the profiles arranged into
1057 groups based on the profiles symmetry (see text for details). The resulting maps that are colour
1058 coded, matching with the profiles, based on the throw profiles type (centre left and right,
1059 respectively). The relative abundance of different types is shown in a pie diagram next to the
1060 respective maps. We note that unlike polygonal faults, the faults in our study area show more
1061 symmetrical profiles with depth, indicating less strain connectivity between the faults in the
1062 system.

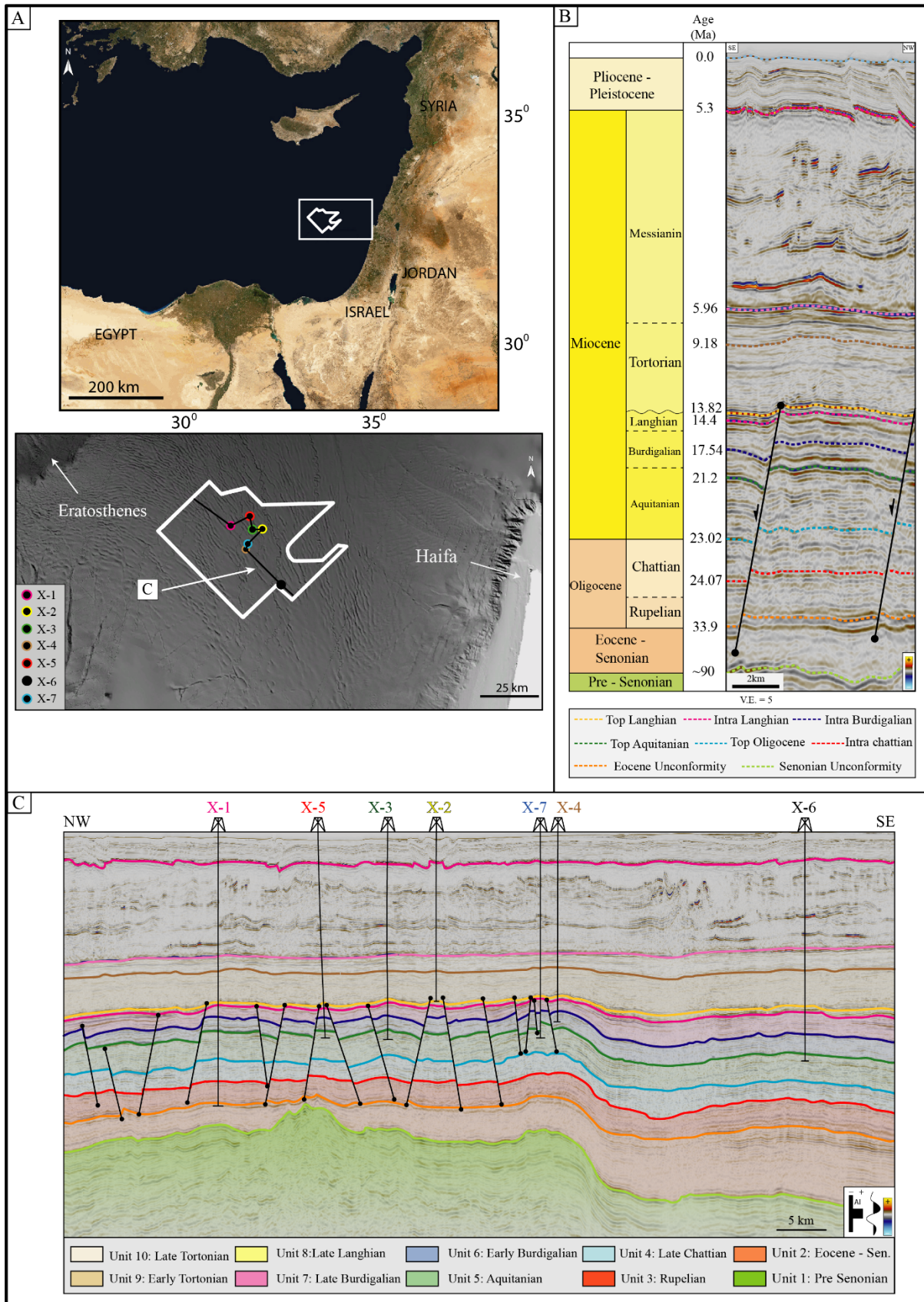
1063 Figure 12: Dip-parallel throw profiles of the same 120 mapped faults. (A) left – all profiles, red
1064 line indicates the average profile. Top Right – TZ1 profiles show a substantial maximum throw
1065 along the Intra-Burdigalian horizon and displacement of the entire Oligocene-Miocene
1066 sedimentary sequence. Bottom Right – TZ2 profiles show similar maximum throw along the
1067 Intra-Burdigalian horizon, but do not reach the Intra-Chattian horizon. (B) An uninterpreted
1068 (left) and an interpreted (right) seismic profile showing TZ1 (blue) and TZ2 (red) faults. The
1069 different TZ's. (C) Geographic location of the TZ in the study area are colour coded, matching
1070 with B, based on the throw profiles type. The relative abundance of different types is shown in
1071 a pie diagram next to the respective map.

1072 Figure 13: (A) An histogram of the Expansion Index measured for the 120 mapped faults along
1073 the eight stratigraphic units (colour coded). Syn-kinematic values are seen for the Late
1074 Burdigalian and late Langhian. Pre-kinematic values for the lower units. (B) Histogram of the
1075 Expansion Index for the TZ1 (left) and for TZ2 (right). Values are in agreement with the
1076 thickness maps and t-z plots, indicating that all the faults in our study area had nucleated during
1077 the Late Burdigalian as syn-depositional faults.

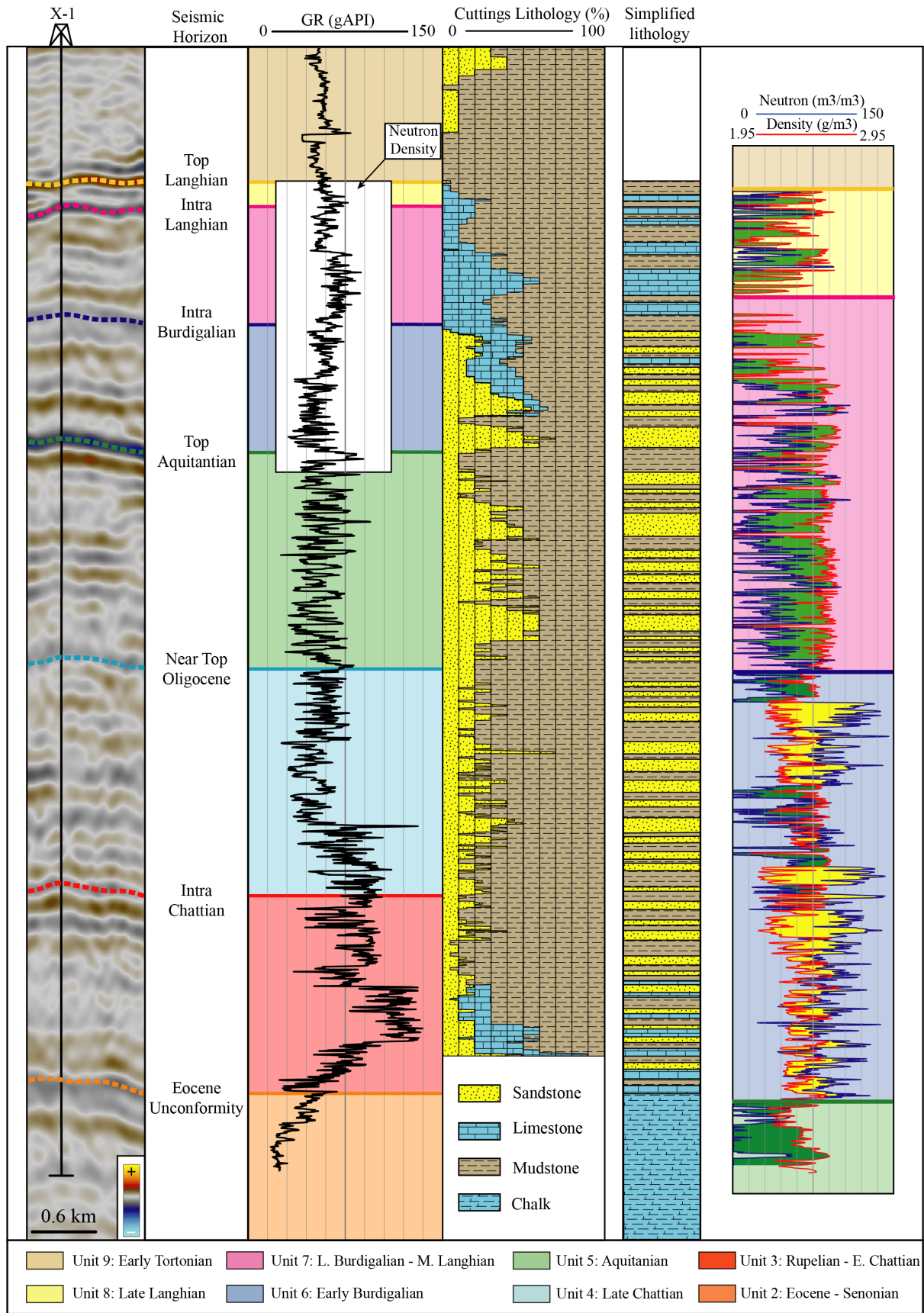
1078 Figure 14: Our mechanical model for the development of the Tertiary layer-bound faults in the
1079 Levant Basin. (A) The state of stress in the early Oligocene, where NW-SE contraction
1080 decreased, allowing isopachous deposition of Unit 3. (B&C) The states of stress developed
1081 with rapid deposition of the sand-dominated units in the Oligocene-Early Miocene, eventually
1082 creating an overpressured Eocene unit and leading to the development of a decollement layer.
1083 (D) Syn-sedimentary faults eventually nucleate during the Late Burdigalian, at the same time
1084 as slip is accommodated along the WSW-ENE-striking strike-slip fault. (E) A sketch
1085 illustrating the different elements in the Levant Basin leading to the development of the NW-
1086 striking normal faults. We propose a differential movement along the WSW-ENE-striking

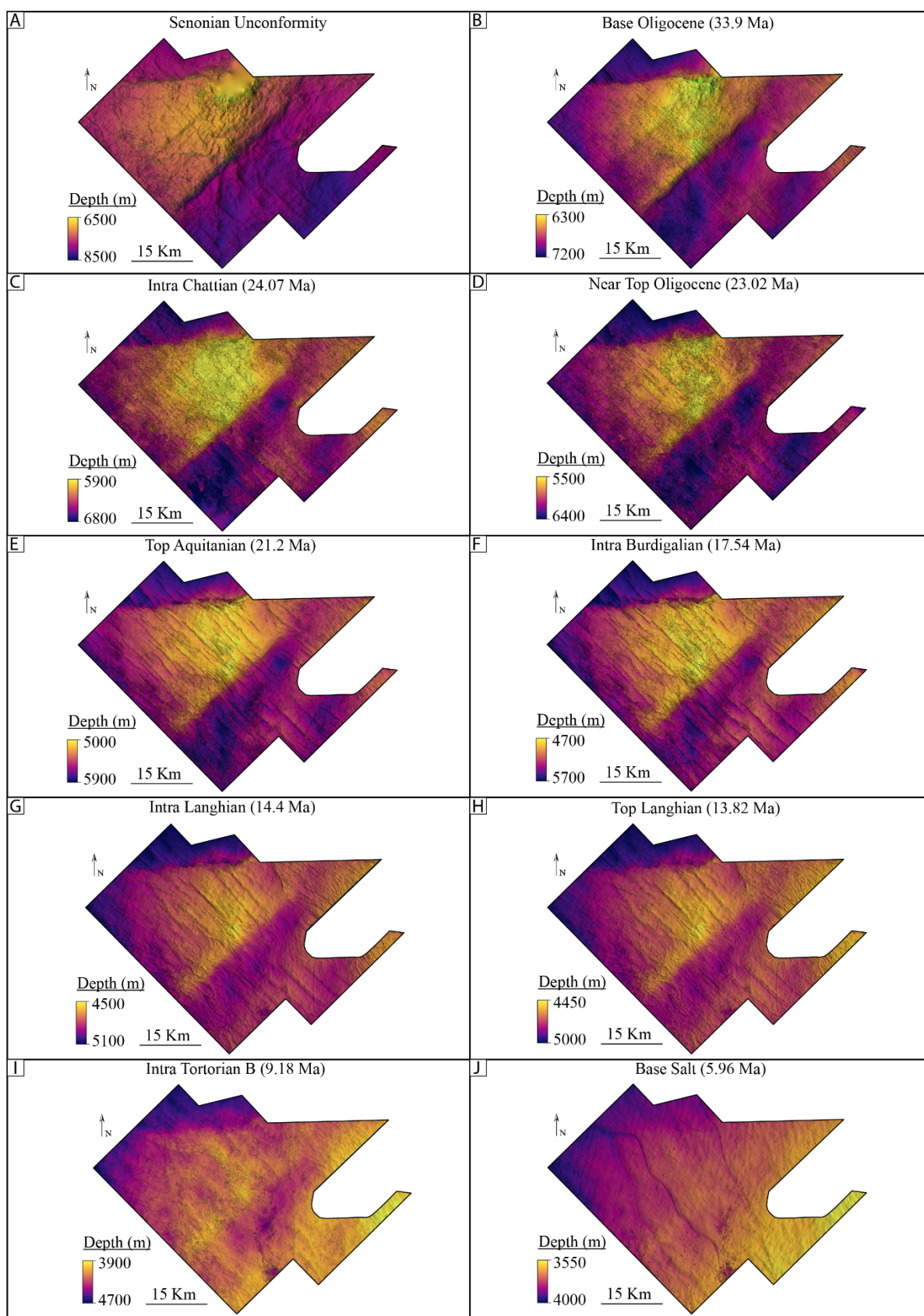
1087 strike-slip faults had caused NE-trending extension, eventually leading to the development of
1088 the layer-bound faults in the Levant Basin. Faults location in the Northern Levant Basin
1089 (dashed blue line) were modified from Ghalayini and Eid (2020) (layer-bound normal faults),
1090 and from Ghalayini et al. (2014) (strike slip faults).

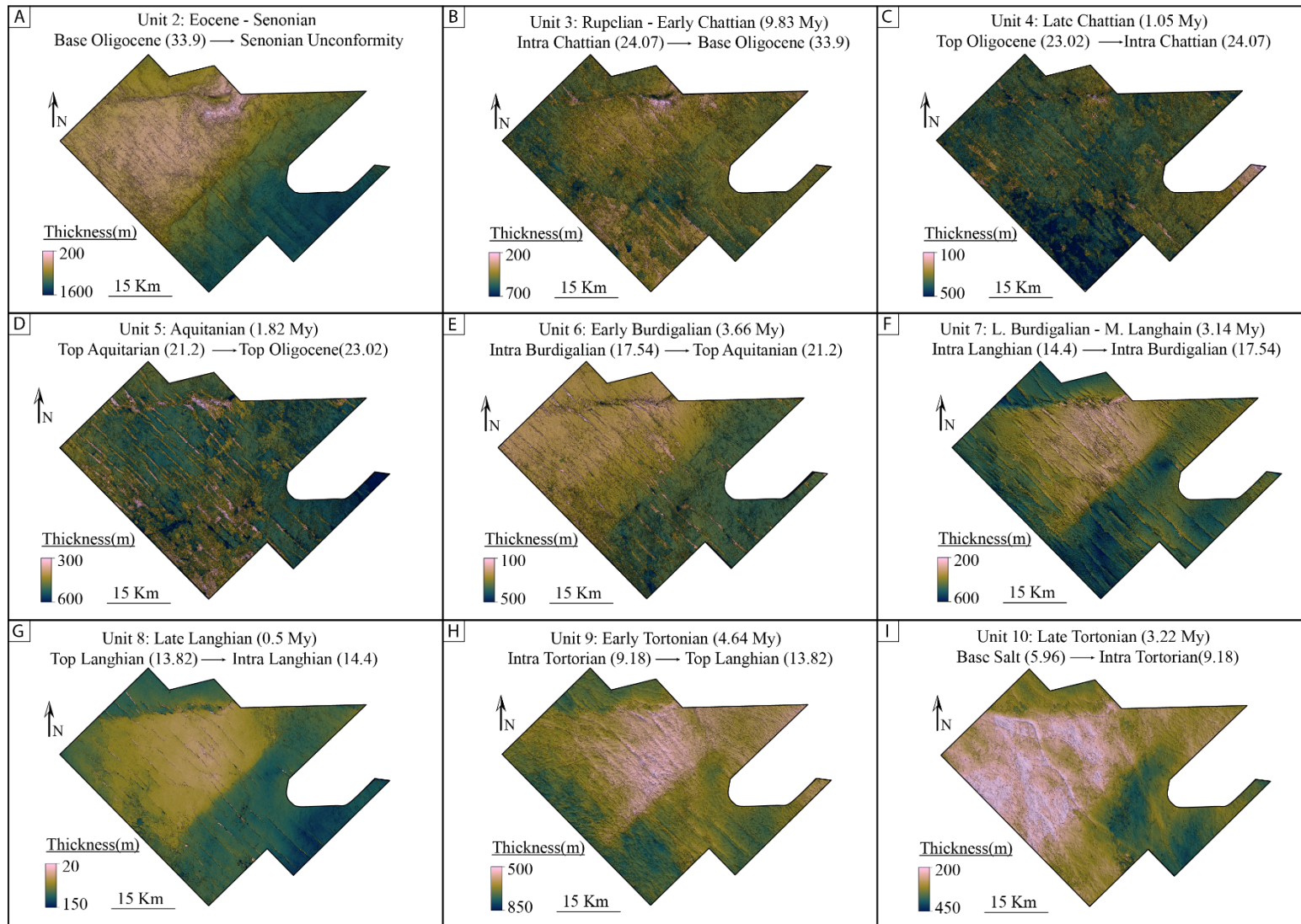




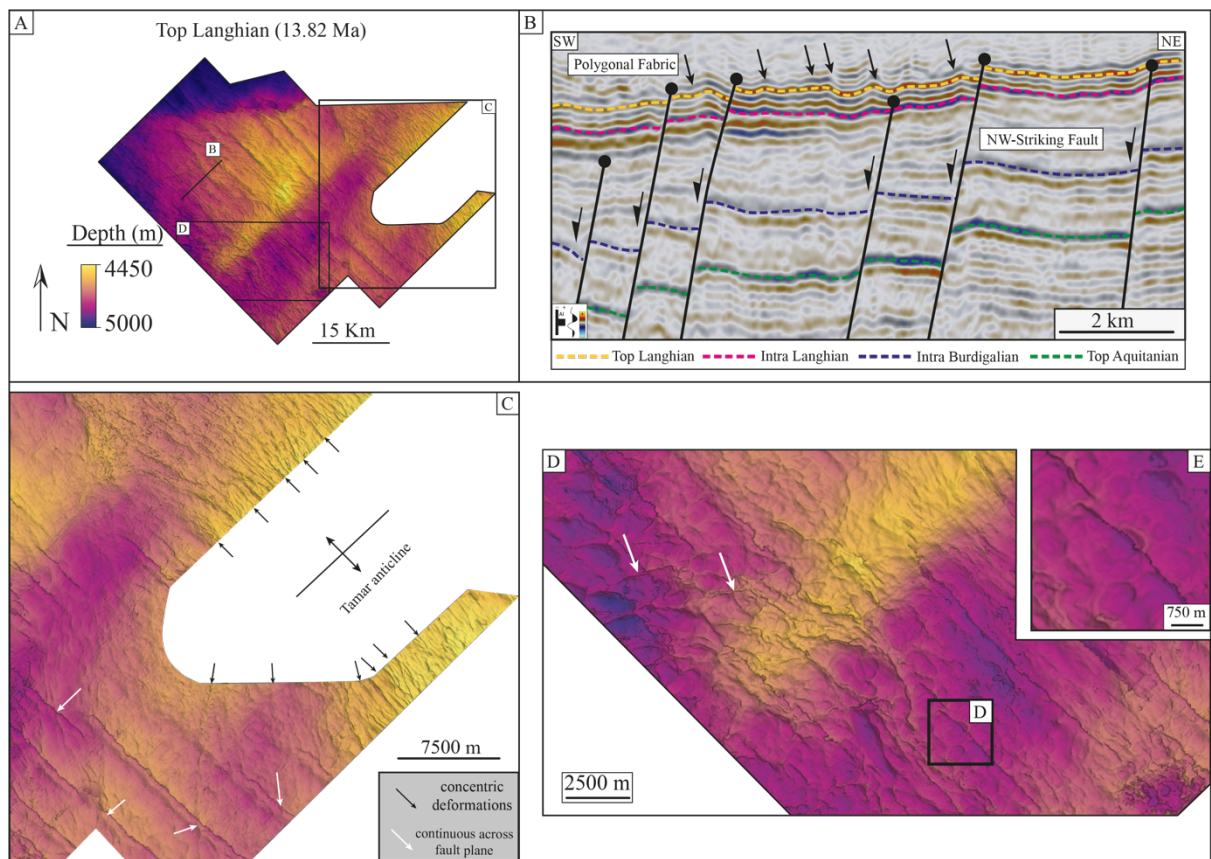
1096 Figure 3







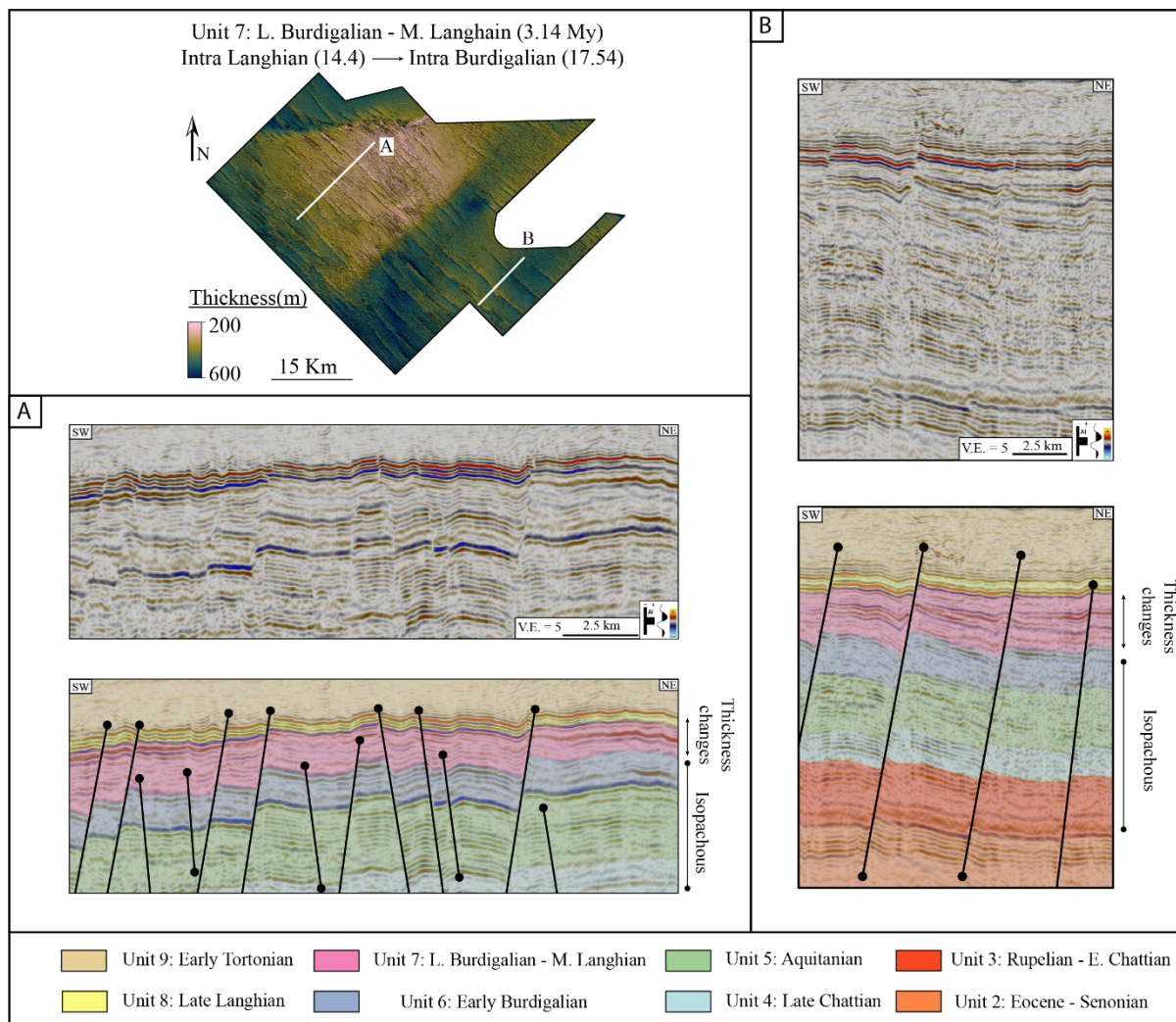
1102 Figure 6



1103

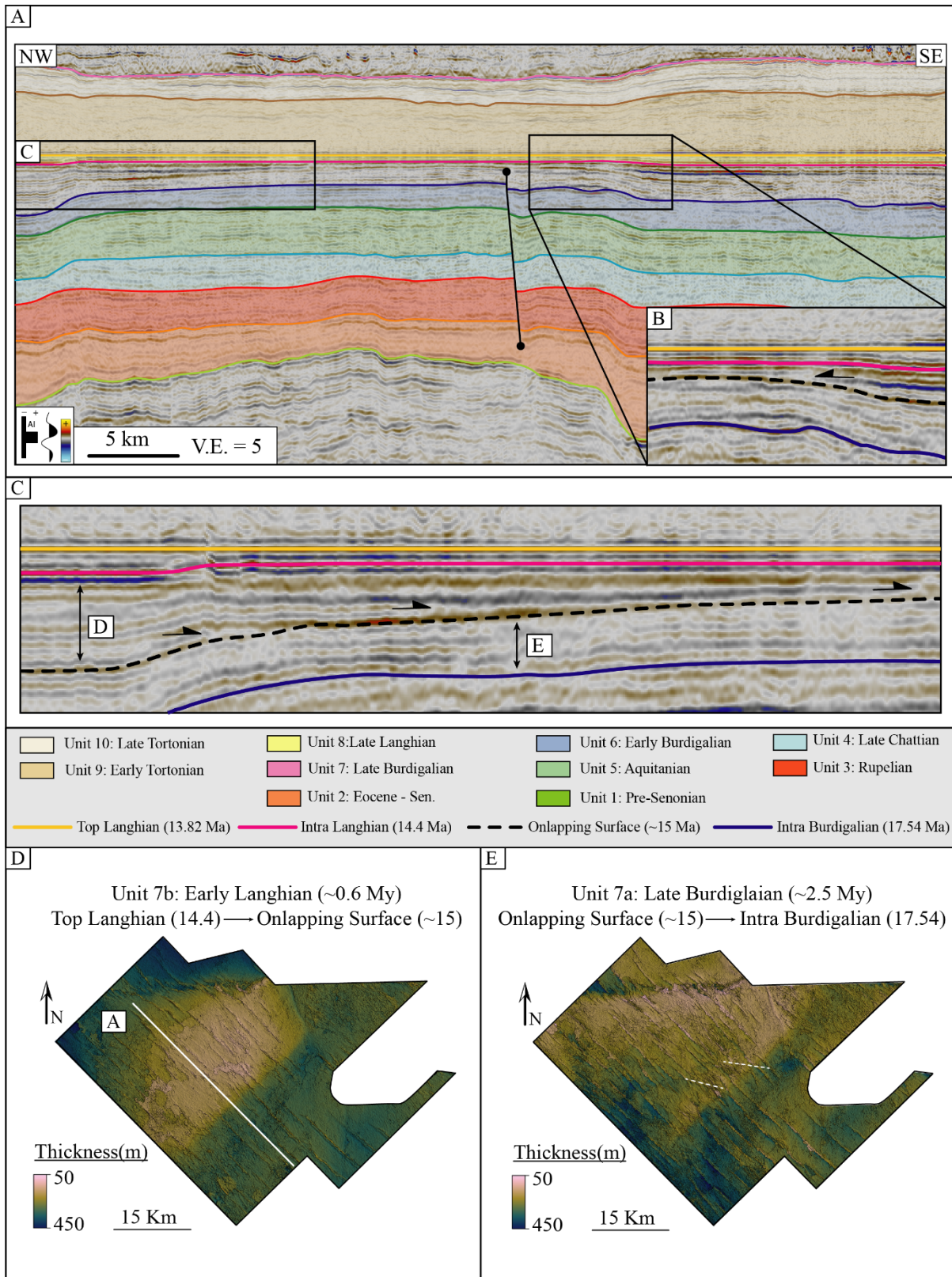
1104 Figure 7

1105



1106

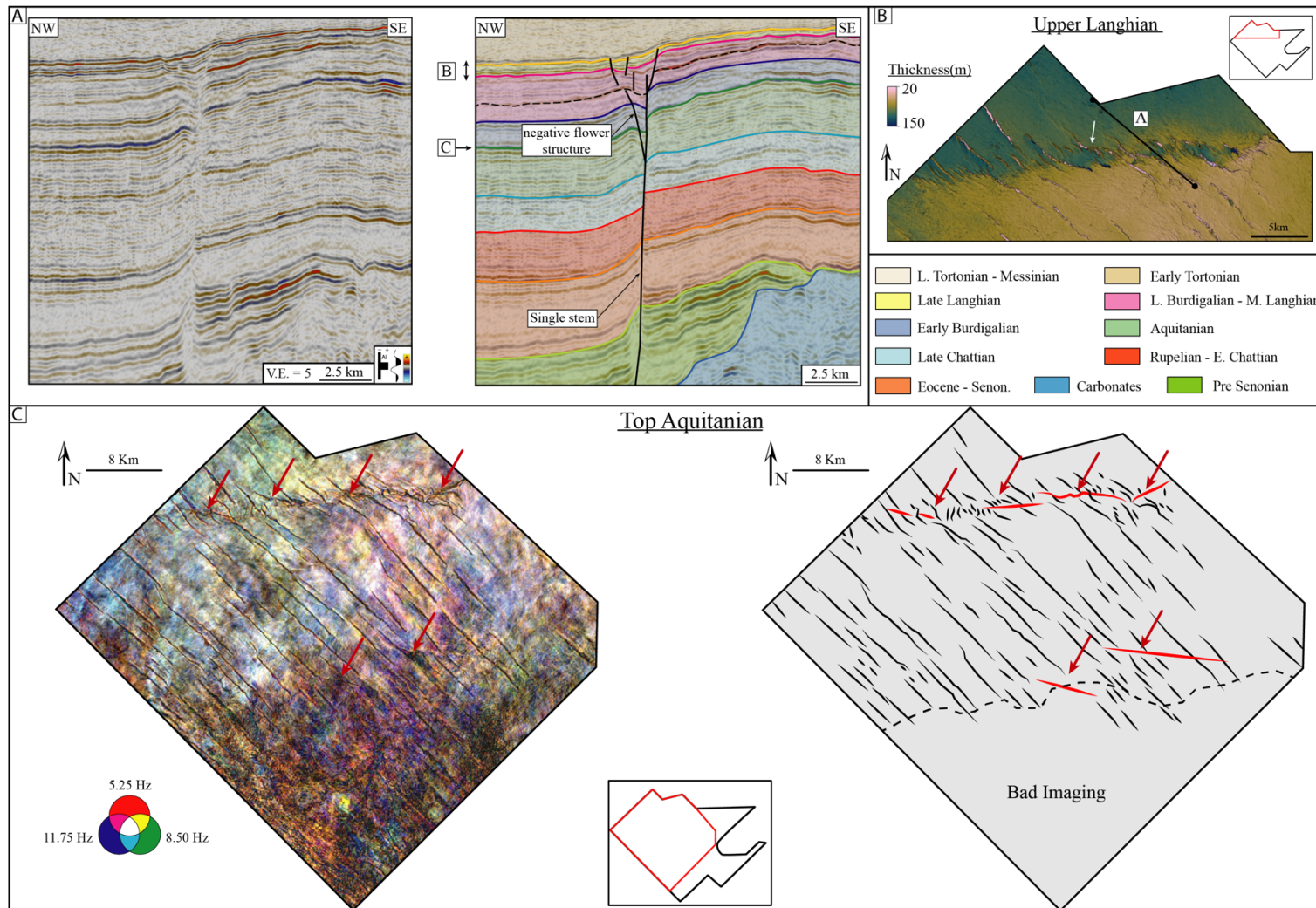
1107 Figure 8



1108

1109

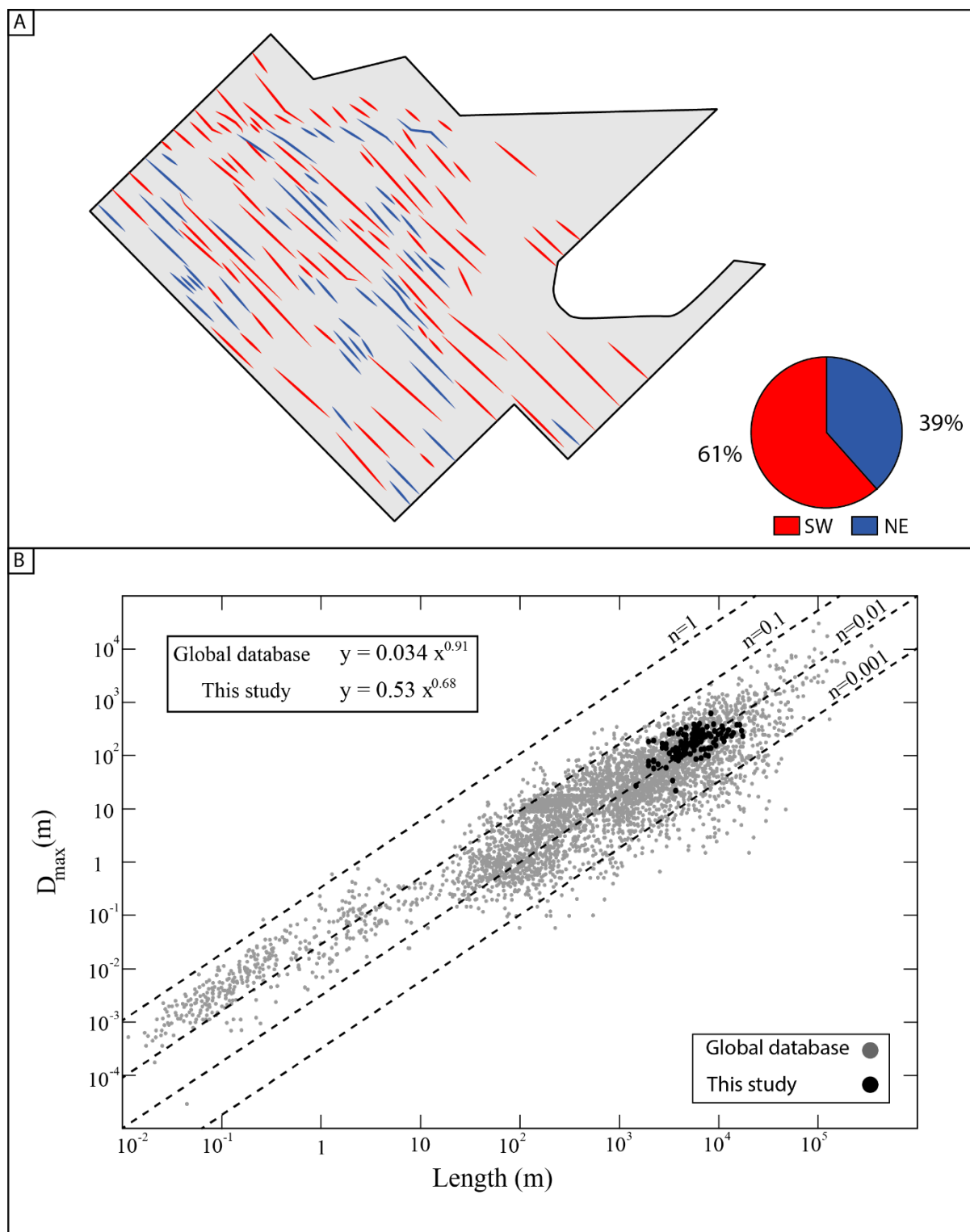
1110 Figure 9



1111

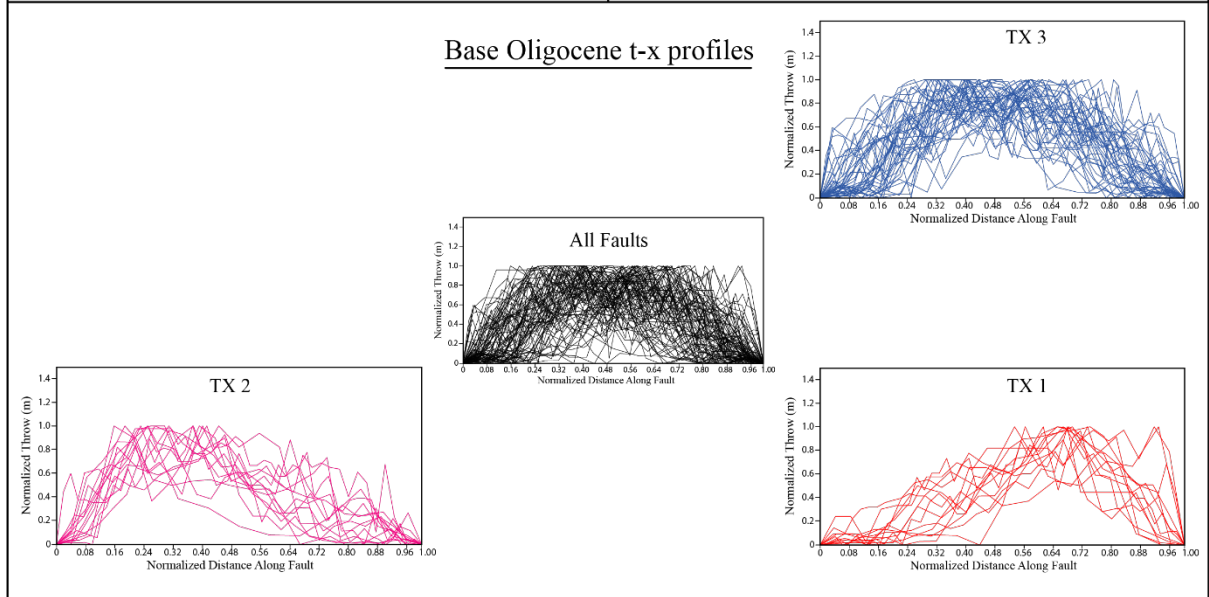
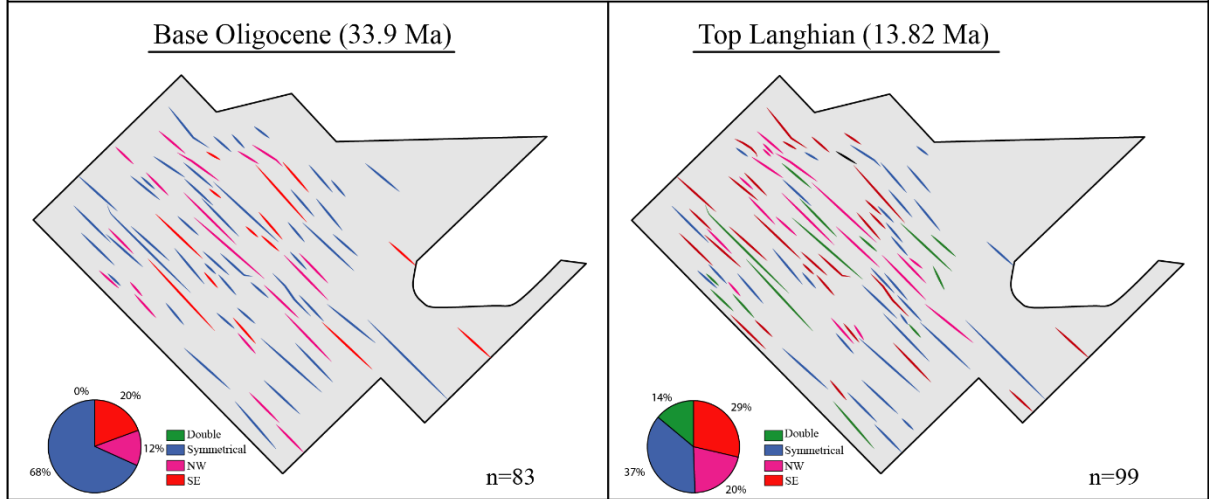
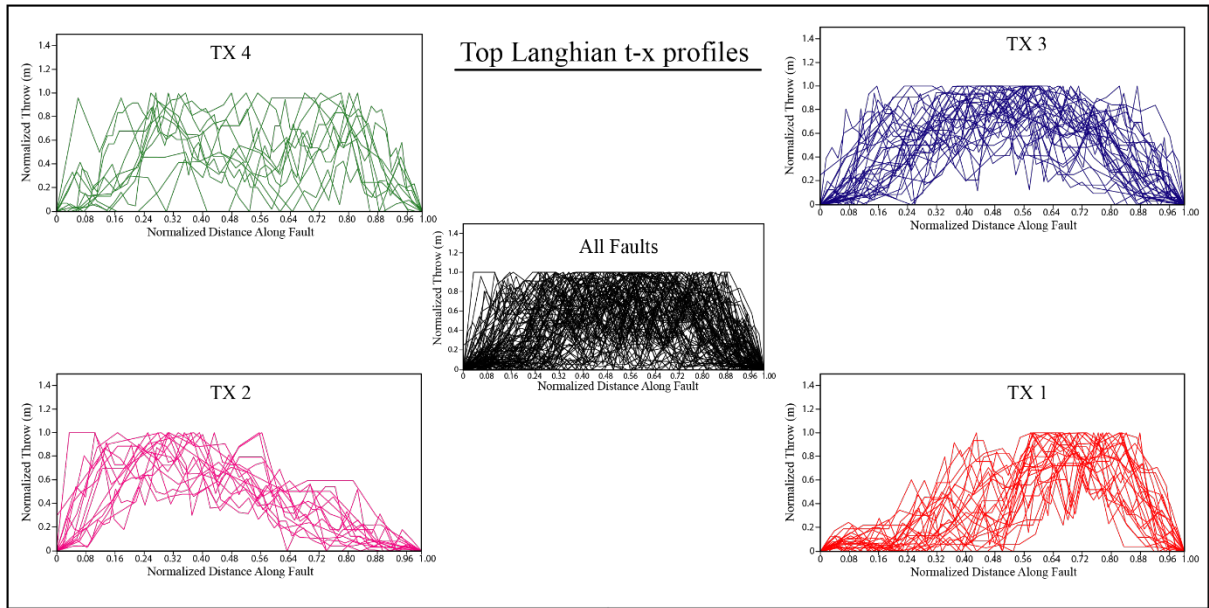
1112

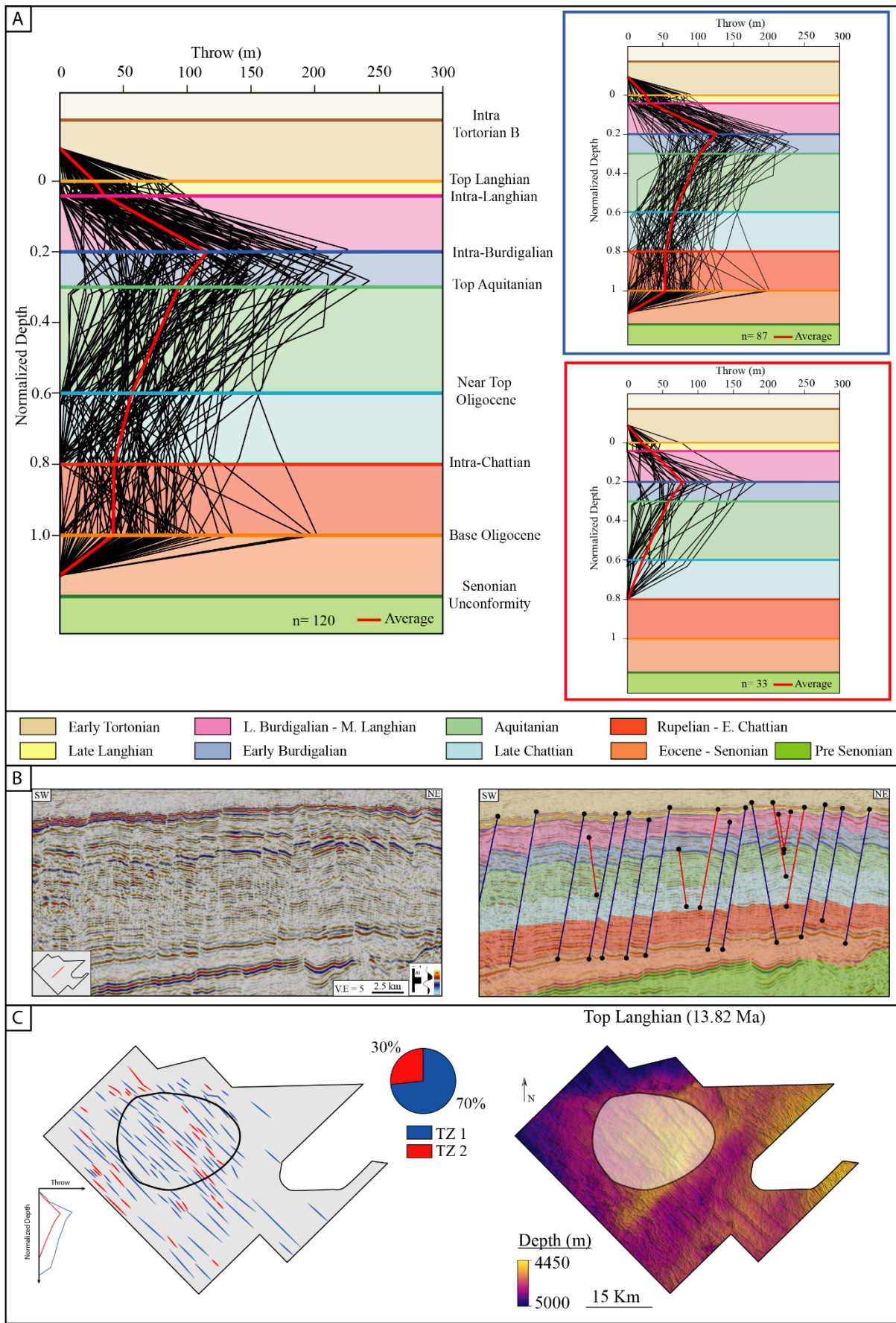
1113 Figure 10

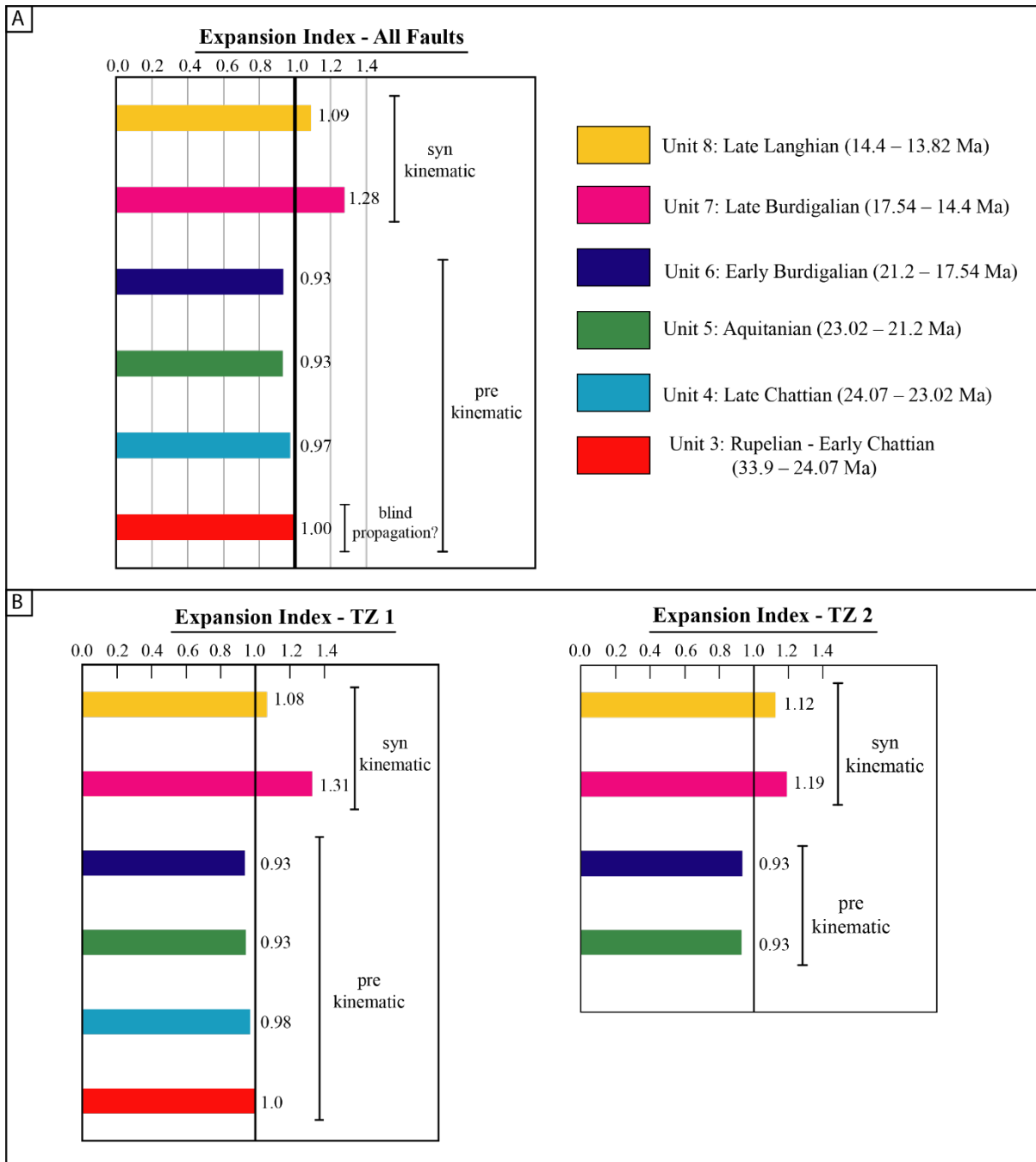


1114

1115

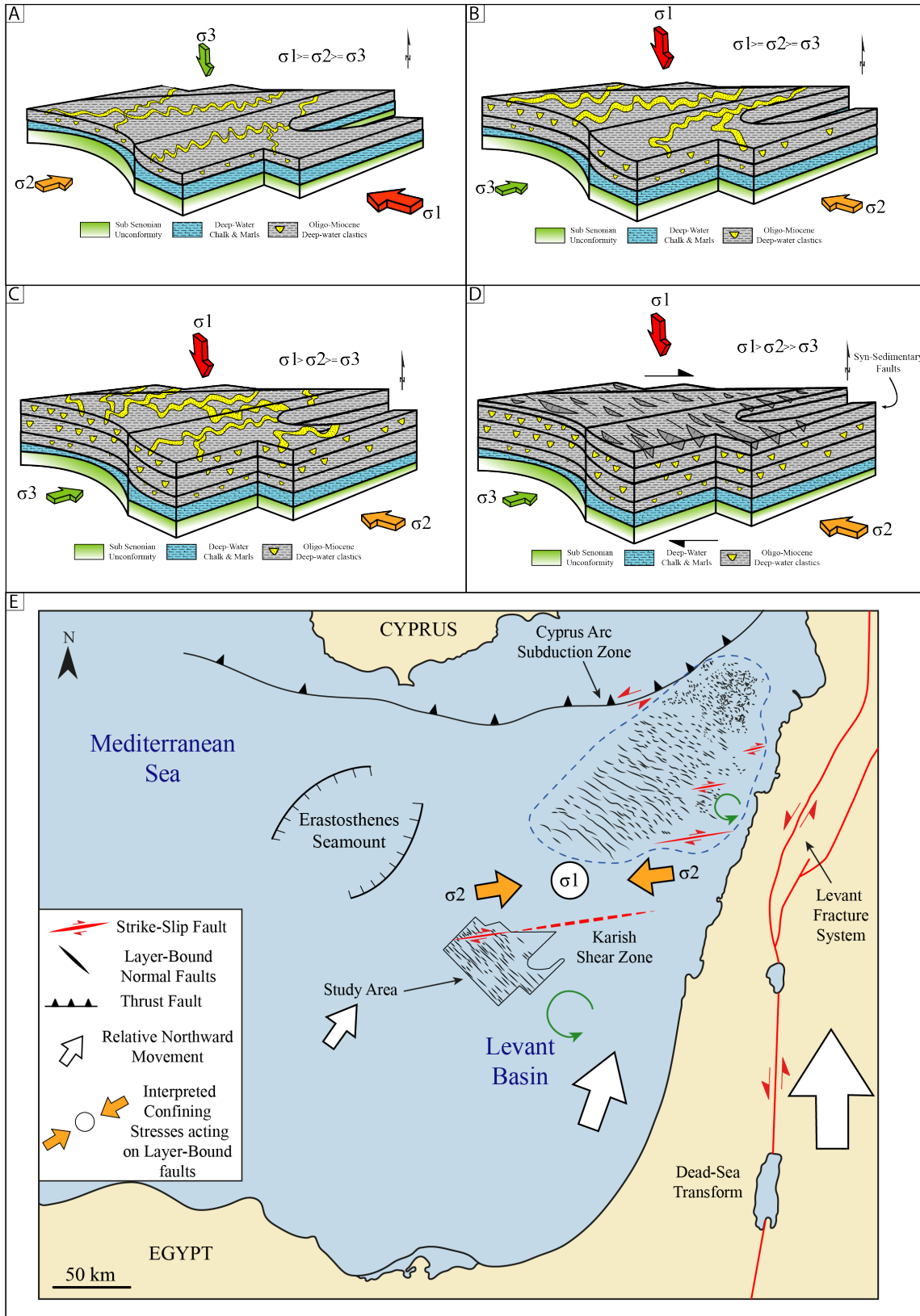






1122

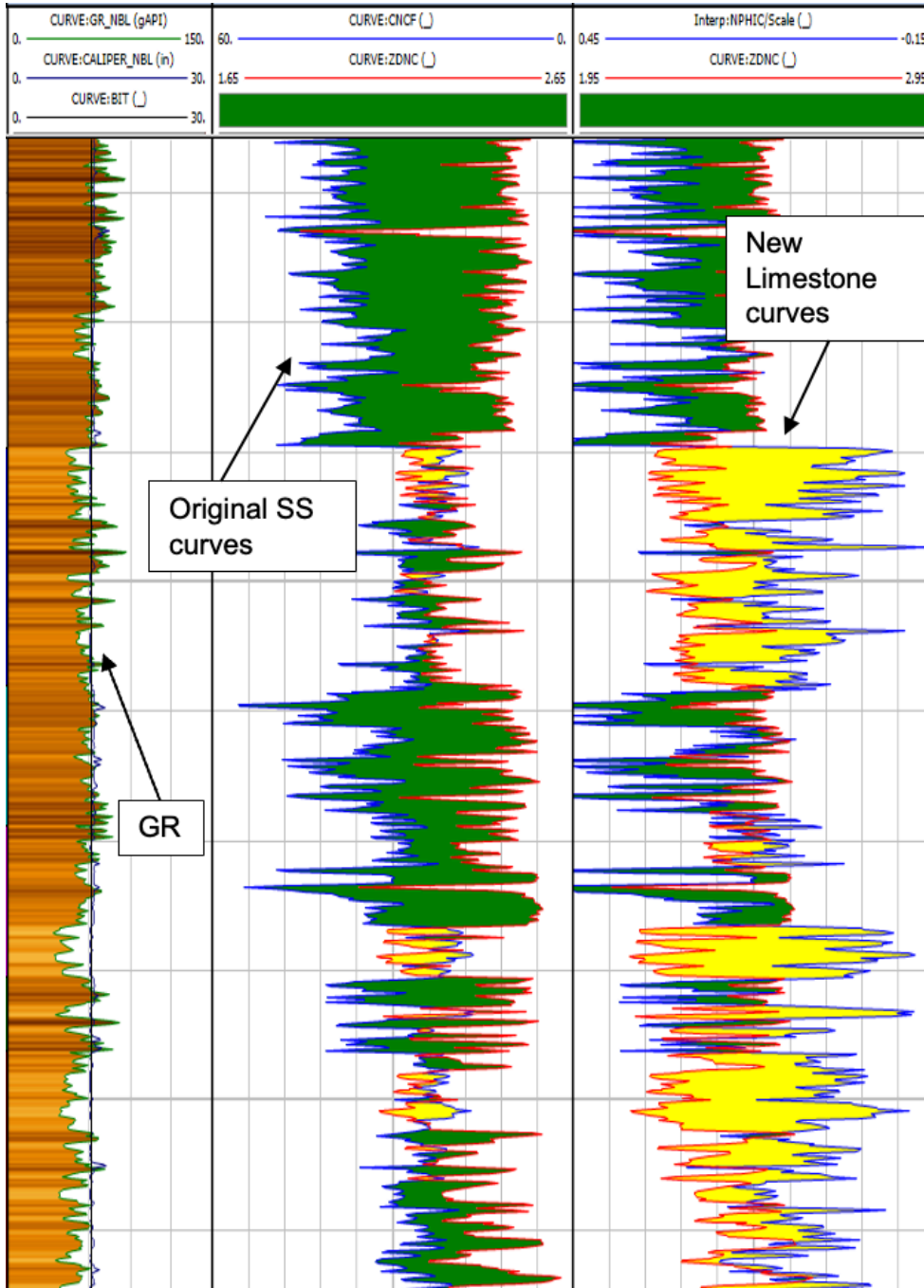
1123



1127 **Supplementary Information**

1128 Neutron Density

1129 Original wireline data provided to this study, and other references (e.g., Christensen and
1130 Powers (2013)), are all sandstone calibrated, and not limestone calibrated as most published
1131 data. To make it easier to the reader to understand the wireline interpretation, we converted the
1132 calibration from sandstone to limestone using IP software.

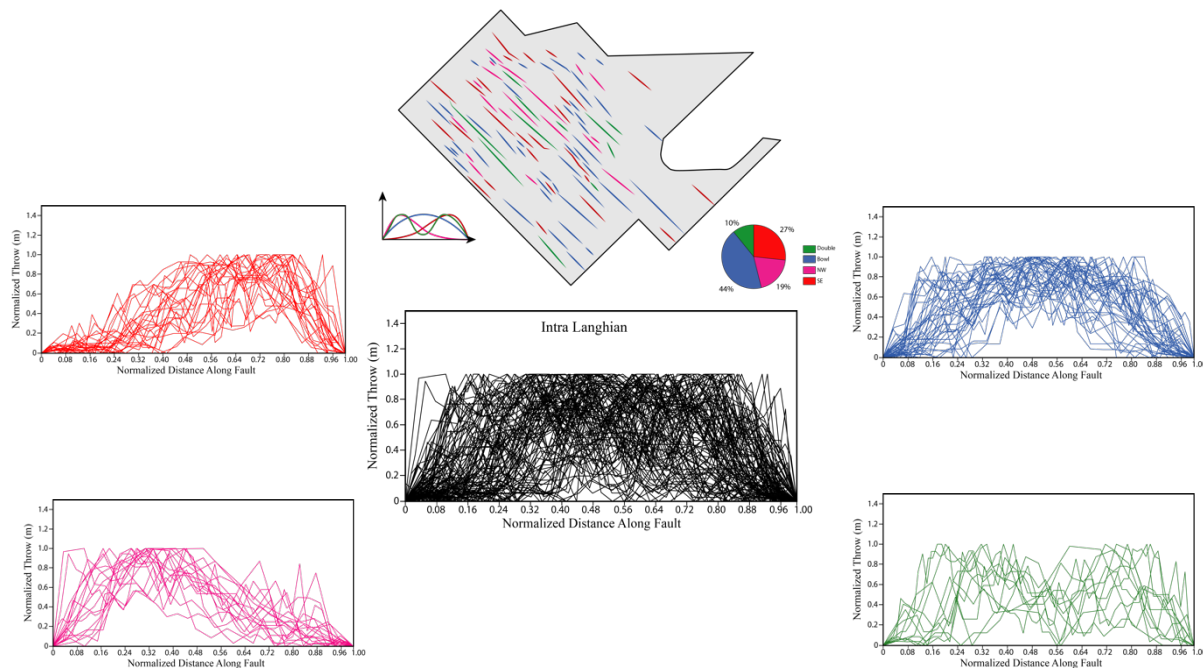


1133

1134

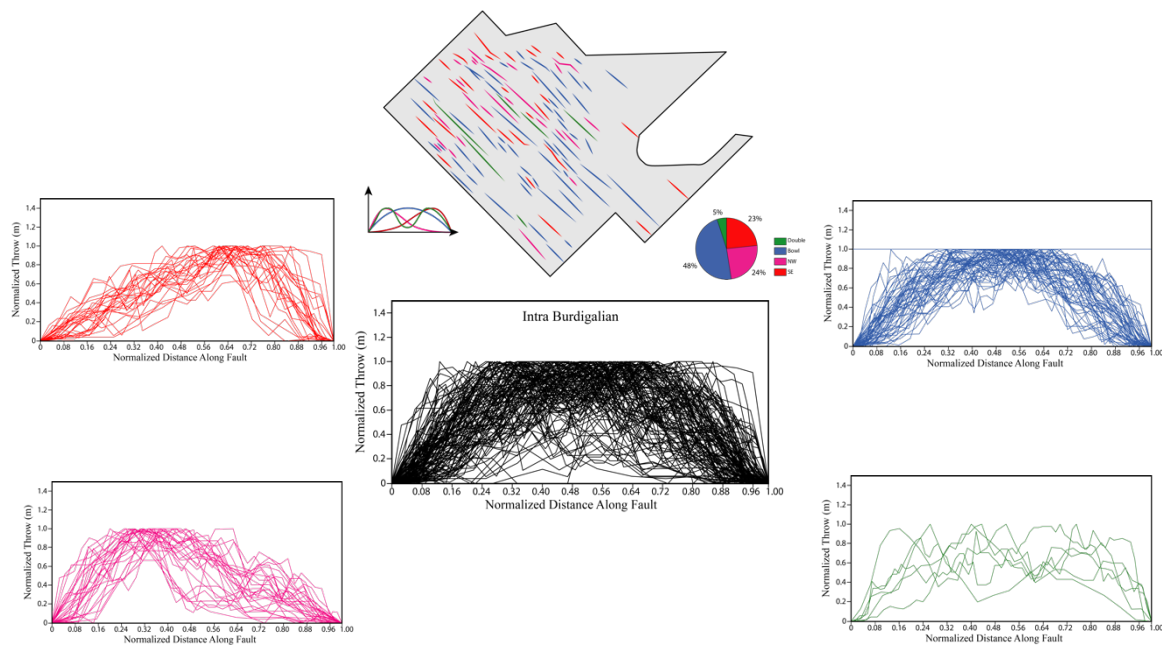
1135 Throw – length (t-x) profiles for each horizon not listed on Figure 11

1136 Intra Langhian horizon



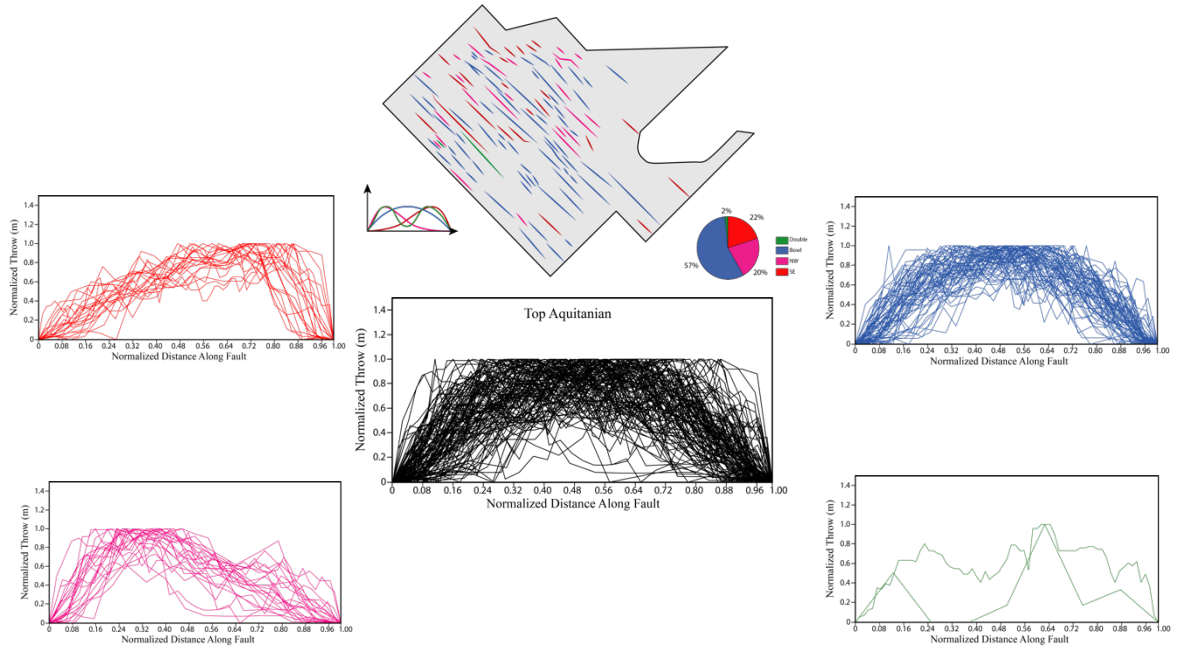
1137

1138 Intra Burdigalian



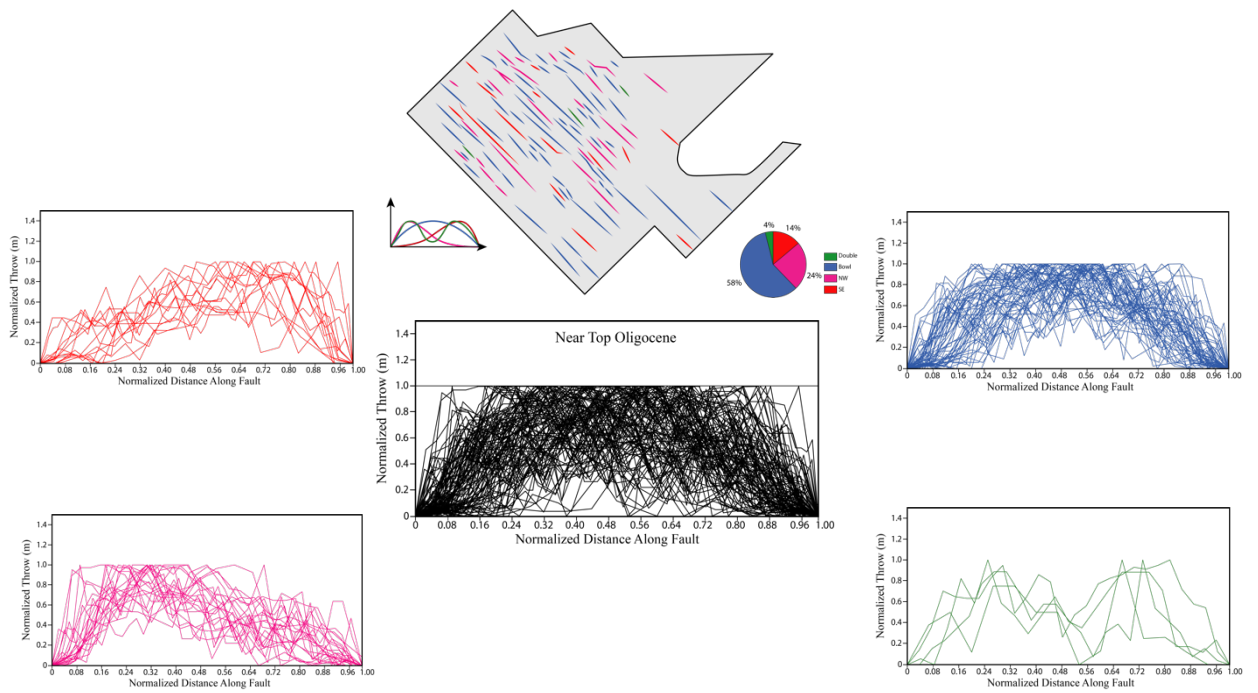
1139

1140 Top Aquitanian



1141

1142 Near Top Oligocene



1143

1144 Intra Chattian

